Measurements of resonant scattering in the Perseus Cluster core with Hitomi SXS*

Hitomi Collaboration, Felix AHARONIAN,[1,2,3] Hiroki AKAMATSU,[4]
Fumie AKIMOTO,[5] Steven W. ALLEN,[6,7,8] Lorella ANGELINI,[9] Marc AUDARD,[10]
Hisamitsu AWAKI,[11] Magnus AXELSSON,[12] Aya BAMBA,[13,14]
Marshall W. BAUTZ,[15] Roger BLANDFORD,[6,7,8] Laura W. BRENNEMAN,[16]
Gregory V. BROWN,[17] Esra BULBUL,[15] Edward M. CACKETT,[18]
Maria CHERNYAKOVA,[1] Meng P. CHIAO,[9] Paolo S. COPPI,[19,20] Elisa COSTANTINI,[4]
Jelle DE PLAA,[4] Cor P. DE VRIES,[4] Jan-Willem DEN HERDER,[4] Chris DONE,[21]
Tadayasu DOTANI,[22] Ken EBISAWA,[22] Megan E. ECKART,[9] Teruaki ENOTO,[23,24]
Yuichiro EZOE,[25] Andrew C. FABIAN,[26] Carlo FERRIGNO,[10] Adam R. FOSTER,[16]
Ryuichi FUJIMOTO,[27] Yasushi FUKAZAWA,[28] Maki FURUKAWA,[59]
Akihiro FURUZAWA,[29] Massimiliano GALEAZZI,[30] Luigi C. GALLO,[31]
Poshak GANDHI,[32] Margherita GIUSTINI,[4] Andrea GOLDWURM,[33,34] Liyi GU,[4]
Matteo GUAINAZZI,[35] Yoshito HABA,[36] Kouichi HAGINO,[37] Kenji HAMAGUCHI,[9,38]
Ilana M. HARRUS,[9,38] Isamu HATSUKADE,[39] Katsuhiro HAYASHI,[22,40]
Takayuki HAYASHI,[40] Kiyoshi HAYASHIDA,[41] Junko S. HIRAGA,[42]
Ann HORNSCHEMEIER,[9] Akio HOSHINO,[43] John P. HUGHES,[44] Yuto ICHINOHE,[25]
Ryo IIZUKA,[22] Hajime INOUE,[45] Yoshiyuki INOUE,[22] Manabu ISHIDA,[22]
Kumi ISHIKAWA,[22] Yoshitaka ISHISAKI,[25] Masachika IWAI,[22] Jelle KAASTRA,[4,46]
Tim KALLMAN,[9] Tsuneyoshi KAMAE,[13] Jun KATAOKA,[47] Satoru KATSUDA,[48]
Nobuyuki KAWAI,[49] Richard L. KELLEY,[9] Caroline A. KILBOURNE,[9]
Takao KITAGUCHI,[28] Shunji KITAMOTO,[43] Tetsu KITAYAMA,[50]
Takayoshi KOHMURA,[37] Motohide KOKUBUN,[22] Katsuji KOYAMA,[51]
Shu KOYAMA,[22] Peter KRETSCHMAR,[52] Hans A. KRIMM,[53,54] Aya KUBOTA,[55]
Hideyo KUNIEDA,[40] Philippe LAURENT,[33,34] Shiu-Hang LEE,[23]
Maurice A. LEUTENEGGER,[9] Olivier O. LIMOUSIN,[34] Michael LOEWENSTEIN,[9,56]
Knox S. LONG,[57] David LUMB,[35] Greg MADEJSKI,[6] Yoshitomo MAEDA,[22]
Daniel MAIER,[33,34] Kazuo MAKISHIMA,[58] Maxim MARKEVITCH,[9]
Hironori MATSUMOTO,[41] Kyoko MATSUSHITA,[59] Dan McCAMMON,[60]
Brian R. McNAMARA,[61] Missagh MEHDIPOUR,[4] Eric D. MILLER,[15]
Jon M. MILLER,[62] Shin MINESHIGE,[23] Kazuhisa MITSUDA,[22]
Ikuyuki MITSUISHI,[40] Takuya MIYAZAWA,[63] Tsunefumi MIZUNO,[28,64]
Hideyuki MORI,[9] Koji MORI,[39] Koji MUKAI,[9,38] Hiroshi MURAKAMI,[65]
Richard F. MUSHOTZKY,[56] Takao NAKAGAWA,[22] Hiroshi NAKAJIMA,[41]
Takeshi NAKAMORI,[66] Shinya NAKASHIMA,[58] Kazuhiro NAKAZAWA,[13,14]
Kumiko K. NOBUKAWA,[67] Masayoshi NOBUKAWA,[68] Hirofumi NODA,[69,70]

Hirokazu ODAKA,[6] Anna OGORZALEK,[6,7] Takaya OHASHI,[25] Masanori OHNO,[28] Takashi OKAJIMA,[9] Naomi OTA,[67] Masanobu OZAKI,[22] Frits PAERELS,[71,†] Stéphane PALTANI,[10] Robert PETRE,[9] Ciro PINTO,[26] Frederick S. PORTER,[9] Katja POTTSCHMIDT,[9,38] Christopher S. REYNOLDS,[56] Samar SAFI-HARB,[72] Shinya SAITO,[43] Kazuhiro SAKAI,[9] Toru SASAKI,[59] Goro SATO,[22] Kosuke SATO,[59,†] Rie SATO,[22] Makoto SAWADA,[73] Norbert SCHARTEL,[52] Peter J. SERLEMTSOS,[9] Hiromi SETA,[25] Megumi SHIDATSU,[58] Aurora SIMIONESCU,[22] Randall K. SMITH,[16] Yang SOONG,[9] Łukasz STAWARZ,[74] Yasuharu SUGAWARA,[22] Satoshi SUGITA,[49] Andrew SZYMKOWIAK,[20] Hiroyasu TAJIMA,[5] Hiromitsu TAKAHASHI,[28] Tadayuki TAKAHASHI,[22] Shiníchiro TAKEDA,[63] Yoh TAKEI,[22] Toru TAMAGAWA,[75] Takayuki TAMURA,[22] Takaaki TANAKA,[51] Yasuo TANAKA,[76,22] Yasuyuki T. TANAKA,[28] Makoto S. TASHIRO,[77] Yuzuru TAWARA,[40] Yukikatsu TERADA,[77] Yuichi TERASHIMA,[11] Francesco TOMBESI,[9,38,78] Hiroshi TOMIDA,[22] Yohko TSUBOI,[48] Masahiro TSUJIMOTO,[22] Hiroshi TSUNEMI,[41] Takeshi Go TSURU,[51] Hiroyuki UCHIDA,[51] Hideki UCHIYAMA,[79] Yasunobu UCHIYAMA,[43] Shutaro UEDA,[22] Yoshihiro UEDA,[23] Shiníchiro UNO,[80] C. Megan URRY,[20] Eugenio URSINO,[30] Shin WATANABE,[22] Norbert WERNER,[81,82,28] Dan R. WILKINS,[6] Brian J. WILLIAMS,[57] Shinya YAMADA,[25] Hiroya YAMAGUCHI,[9,56] Kazutaka YAMAOKA,[5,40] Noriko Y. YAMASAKI,[22] Makoto YAMAUCHI,[39] Shigeo YAMAUCHI,[67] Tahir YAQOOB,[9,38] Yoichi YATSU,[49] Daisuke YONETOKU,[27] Irina ZHURAVLEVA,[6,7,†] and Abderahmen ZOGHBI[62]

[1]Dublin Institute for Advanced Studies, 31 Fitzwilliam Place, Dublin 2, Ireland

[2]Max-Planck-Institut für Kernphysik, PO Box 103980, 69029 Heidelberg, Germany

[3]Gran Sasso Science Institute, viale Francesco Crispi, 7 67100 L'Aquila (AQ), Italy

[4]SRON Netherlands Institute for Space Research, Sorbonnelaan 2, 3584 CA Utrecht, The Netherlands

[5]Institute for Space-Earth Environmental Research, Nagoya University, Furo-cho, Chikusa-ku, Nagoya, Aichi 464-8601, Japan

[6]Kavli Institute for Particle Astrophysics and Cosmology, Stanford University, 452 Lomita Mall, Stanford, CA 94305, USA

[7]Department of Physics, Stanford University, 382 Via Pueblo Mall, Stanford, CA 94305, USA

[8]SLAC National Accelerator Laboratory, 2575 Sand Hill Road, Menlo Park, CA 94025, USA

[9]NASA, Goddard Space Flight Center, 8800 Greenbelt Road, Greenbelt, MD 20771, USA

[10]Department of Astronomy, University of Geneva, ch. d'Écogia 16, CH-1290 Versoix, Switzerland

[11]Department of Physics, Ehime University, 2-5 Bunkyo-cho, Matsuyama, Ehime 790-8577, Japan

[12]Department of Physics and Oskar Klein Center, Stockholm University, 106 91 Stockholm, Sweden

[13]Department of Physics, The University of Tokyo, 7-3-1 Hongo, Bunkyo-ku, Tokyo 113-0033, Japan

[14]Research Center for the Early Universe, School of Science, The University of Tokyo, 7-3-1 Hongo, Bunkyo-ku, Tokyo 113-0033, Japan

[15]Kavli Institute for Astrophysics and Space Research, Massachusetts Institute of Technology, 77 Massachusetts Avenue, Cambridge, MA 02139, USA

[16]Smithsonian Astrophysical Observatory, 60 Garden St, MS-4. Cambridge, MA 02138, USA

[17]Lawrence Livermore National Laboratory, 7000 East Avenue, Livermore, CA 94550, USA

[18]Department of Physics and Astronomy, Wayne State University, 666 W. Hancock St, Detroit, MI 48201, USA

[19]Department of Astronomy, Yale University, PO Box 208101, New Haven, CT 06520-8101, USA

[20]Department of Physics, Yale University, New Haven, Box 208120, CT 06520-8120, USA

[21]Centre for Extragalactic Astronomy, Department of Physics, University of Durham, South Road, Durham, DH1 3LE, UK

[22]Japan Aerospace Exploration Agency, Institute of Space and Astronautical Science, 3-1-1 Yoshino-dai, Chuo-ku, Sagamihara, Kanagawa 252-5210, Japan

[23]Department of Astronomy, Kyoto University, Kitashirakawa-Oiwake-cho, Sakyo-ku, Kyoto, Kyoto 606-8502, Japan

[24]The Hakubi Center for Advanced Research, Kyoto University, Yoshida-honmachi, Sakyo-ku, Kyoto, Kyoto 606-8501, Japan

[25]Department of Physics, Tokyo Metropolitan University, 1-1 Minami-Osawa, Hachioji, Tokyo 192-0397, Japan

[26]Institute of Astronomy, University of Cambridge, Madingley Road, Cambridge, CB3 0HA, UK

[27]Faculty of Mathematics and Physics, Kanazawa University, Kakuma-machi, Kanazawa, Ishikawa 920-1192, Japan

[28]School of Science, Hiroshima University, 1-3-1 Kagamiyama, Higashi-Hiroshima, Hiroshima 739-8526, Japan

[29]Fujita Health University, 1-98 Dengakugakubo, Kutsukake-cho, Toyoake, Aichi 470-1192, Japan

[30]Physics Department, University of Miami, 1320 Campo Sano Dr., Coral Gables, FL 33146, USA

[31]Department of Astronomy and Physics, Saint Mary's University, 923 Robie Street, Halifax, NS, B3H 3C3, Canada

[32]Department of Physics and Astronomy, University of Southampton, Highfield, Southampton, SO17 1BJ, UK

[33]Laboratoire APC, 10 rue Alice Domon et Léonie Duquet, 75013 Paris, France

[34]CEA Saclay, 91191 Gif sur Yvette, France

[35]European Space Research and Technology Center, Keplerlaan 1 2201 AZ Noordwijk, The Netherlands

[36]Department of Physics and Astronomy, Aichi University of Education, 1 Hirosawa, Igaya-cho, Kariya, Aichi 448-8543, Japan

[37]Department of Physics, Tokyo University of Science, 2641 Yamazaki, Noda, Chiba 278-8510, Japan

[38]Department of Physics, University of Maryland Baltimore County, 1000 Hilltop Circle, Baltimore, MD 21250, USA

[39]Department of Applied Physics and Electronic Engineering, University of Miyazaki, 1-1 Gakuen Kibanadai-Nishi, Miyazaki, Miyazaki 889-2192, Japan

[40]Department of Physics, Nagoya University, Furo-cho, Chikusa-ku, Nagoya, Aichi 464-8602, Japan

[41]Department of Earth and Space Science, Osaka University, 1-1 Machikaneyama-cho, Toyonaka, Osaka 560-0043, Japan

[42]Department of Physics, Kwansei Gakuin University, 2-1 Gakuen, Sanda, Hyogo 669-1337, Japan

[43]Department of Physics, Rikkyo University, 3-34-1 Nishi-Ikebukuro, Toshima-ku, Tokyo 171-8501, Japan

[44]Department of Physics and Astronomy, Rutgers University, 136 Frelinghuysen Road, Piscataway, NJ 08854, USA

[45]Meisei University, 2-1-1 Hodokubo, Hino, Tokyo 191-8506, Japan

[46]Leiden Observatory, Leiden University, PO Box 9513, 2300 RA Leiden, The Netherlands

[47]Research Institute for Science and Engineering, Waseda University, 3-4-1 Ohkubo, Shinjuku-ku, Tokyo 169-8555, Japan

[48]Department of Physics, Chuo University, 1-13-27 Kasuga, Bunkyo-ku, Tokyo 112-8551, Japan

[49]Department of Physics, Tokyo Institute of Technology, 2-12-1 Ookayama, Meguro-ku, Tokyo 152-8550, Japan

[50]Department of Physics, Toho University, 2-2-1 Miyama, Funabashi, Chiba 274-8510, Japan

[51]Department of Physics, Kyoto University, Kitashirakawa-Oiwake-cho, Sakyo-ku, Kyoto, Kyoto 606-8502, Japan

[52]European Space Astronomy Center, Camino Bajo del Castillo, s/n., 28692 Villanueva de la Cañada, Madrid, Spain

[53]Universities Space Research Association, 7178 Columbia Gateway Drive, Columbia, MD 21046, USA

[54]National Science Foundation, 4201 Wilson Blvd, Arlington, VA 22230, USA

[55]Department of Electronic Information Systems, Shibaura Institute of Technology, 307 Fukasaku, Minuma-ku, Saitama, Saitama 337-8570, Japan

[56]Department of Astronomy, University of Maryland, College Park, MD 20742, USA

[57]Space Telescope Science Institute, 3700 San Martin Drive, Baltimore, MD 21218, USA

[58]Institute of Physical and Chemical Research, 2-1 Hirosawa, Wako, Saitama 351-0198, Japan

[59]Department of Physics, Tokyo University of Science, 1-3 Kagurazaka, Shinjuku-ku, Tokyo 162-8601, Japan

[60]Department of Physics, University of Wisconsin, Madison, WI 53706, USA

[61]Department of Physics and Astronomy, University of Waterloo, 200 University Avenue West, Waterloo, Ontario, N2L 3G1, Canada

[62]Department of Astronomy, University of Michigan, 1085 South University Avenue, Ann Arbor, MI 48109, USA

[63]Okinawa Institute of Science and Technology Graduate University, 1919-1 Tancha, Onna-son, Kunigami-gun, Okinawa 904-0495, Japan

[64]Hiroshima Astrophysical Science Center, Hiroshima University, 1-3-1 Kagamiyama, Higashi-Hiroshima, Hiroshima 739-8526, Japan

[65]Faculty of Liberal Arts, Tohoku Gakuin University, 2-1-1 Tenjinzawa, Izumi-ku, Sendai, Miyagi 981-3193, Japan

[66]Faculty of Science, Yamagata University, 1-4-12 Kojirakawa-machi, Yamagata, Yamagata 990-8560, Japan

[67]Department of Physics, Nara Women's University, Kitauoyanishi-machi, Nara, Nara 630-8506, Japan

[68]Department of Teacher Training and School Education, Nara University of Education, Takabatake-cho, Nara, Nara 630-8528, Japan

[69]Frontier Research Institute for Interdisciplinary Sciences, Tohoku University, 6-3 Aramakiazaaoba, Aoba-ku, Sendai, Miyagi 980-8578, Japan

[70]Astronomical Institute, Tohoku University, 6-3 Aramakiazaaoba, Aoba-ku, Sendai, Miyagi 980-8578, Japan

[71]Astrophysics Laboratory, Columbia University, 550 West 120th Street, New York, NY 10027, USA

[72]Department of Physics and Astronomy, University of Manitoba, Winnipeg, MB R3T 2N2, Canada

[73]Department of Physics and Mathematics, Aoyama Gakuin University, 5-10-1 Fuchinobe, Chuo-ku, Sagamihara, Kanagawa 252-5258, Japan

[74]Astronomical Observatory of Jagiellonian University, ul. Orla 171, 30-244 Kraków, Poland

[75]RIKEN Nishina Center, 2-1 Hirosawa, Wako, Saitama 351-0198, Japan

[76]Max-Planck-Institut für extraterrestrische Physik, Giessenbachstrasse 1, 85748 Garching , Germany

[77]Department of Physics, Saitama University, 255 Shimo-Okubo, Sakura-ku, Saitama 338-8570, Japan

[78]Department of Physics, University of Rome "Tor Vergata", Via della Ricerca Scientifica 1, I-00133 Rome, Italy

[79]Faculty of Education, Shizuoka University, 836 Ohya, Suruga-ku, Shizuoka 422-8529, Japan

[80]Faculty of Health Sciences, Nihon Fukushi University , 26-2 Higashi Haemi-cho, Handa, Aichi 475-0012, Japan

[81]MTA-Eötvös University Lendület Hot Universe Research Group, Pázmány Péter sétány 1/A, Budapest, 1117, Hungary

[82]Department of Theoretical Physics and Astrophysics, Faculty of Science, Masaryk University, Kotlářská 2, Brno, 611 37, Czech Republic

*The corresponding authors are Kosuke Sato, Irina Zhuravleva, Frits Paerels, Maki Furukawa, Masanori Ohno, Megan E. Eckart, Akihiro Furuzawa, Caroline A. Kilbourne, and Maurice A. Leutenegger.

†E-mail: ksato@rs.tus.ac.jp, ksksato@phy.saitama-u.ac.jp, zhur@stanford.edu, frits.paerels@gmail.com

Abstract

Thanks to its high spectral resolution (∼5 eV at 6 keV), the Soft X-ray Spectrometer (SXS) on board Hitomi enables us to measure the detailed structure of spatially resolved emission lines from highly ionized ions in galaxy clusters for the first time. In this series of papers, using the SXS we have measured the velocities of gas motions, metallicities and the multi-temperature structure of the gas in the core of the Perseus Cluster. Here, we show that when inferring physical properties from line emissivities in systems like Perseus, the resonant scattering effect should be taken into account. In the Hitomi waveband, resonant scattering mostly affects the Fe xxv Heα line (*w*)—the strongest line in the spectrum. The flux measured by Hitomi in this line is suppressed by a factor of ∼1.3 in the inner ∼30 kpc, compared to predictions for an optically thin plasma; the suppression decreases with the distance from the center. The *w* line also appears slightly broader than other lines from the same ion. The observed distortions of the *w* line flux, shape, and distance dependence are all consistent with the expected effect of the resonant scattering in the Perseus core. By measuring the ratio of fluxes in optically thick (*w*) and thin (Fe xxv forbidden, Heβ, Lyα) lines, and comparing these ratios with predictions from Monte Carlo radiative transfer simulations, the velocities of gas motions have been obtained. The results are consistent with the direct measurements of gas velocities from line broadening described elsewhere in this series, although the systematic and statistical uncertainties remain significant. Further improvements in the predictions of line emissivities in plasma models, and deeper observations with future X-ray missions offering similar or better capabilities to the Hitomi SXS, will enable resonant scattering measurements to provide powerful constraints on the amplitude and anisotropy of cluster gas motions.

Key words: galaxies: clusters: individual (Perseus Cluster) — galaxies: clusters: intracluster medium — X-rays: galaxies: clusters

1 Introduction

The hot (10^7–10^8 K) gas in the intracluster medium (ICM) is optically thin to the continuum X-ray radiation, meaning that galaxy clusters are transparent to their own X-ray continuum photons. However, Gilfanov, Syunyaev, and Churazov ([1987](#)) showed that the strongest X-ray resonance lines can have significant optical depths, of order unity or larger. Line photons can therefore undergo resonant scattering (hereafter RS), that is, they can be absorbed by ions and then almost instantaneously re-emitted in a different direction. As a result of this scattering, the emission line intensity is reduced in the direction of the center of the cluster (generally the region of largest optical depth along our line of sight), and enhanced towards the outskirts (e.g., see review by Churazov et al. [2010](#)). Even if the RS effect is not strong, it will affect the spatially resolved measurement of elemental abundances in the ICM (e.g., Böhringer et al. [2001](#); Sanders et al. [2004](#)), distort the profiles of X-ray surface brightness (e.g., Gilfanov et al. [1987](#); Shigeyama [1998](#)), and can lead to up to tens of percent

polarization of the line radiation (Sazonov et al. [2002](#); Zhuravleva et al. [2010](#)).

There have been numerous attempts to detect the RS effect in X-ray spectra of the Perseus Cluster (e.g., Molendi et al. [1998](#); Ezawa et al. [2001](#); Churazov et al. [2004](#)) and other clusters (e.g., Kaastra et al. [1999](#); Akimoto et al. [2000](#); Mathews et al. [2001](#); Sakelliou et al. [2002](#); Sanders & Fabian [2006](#)). However, the results remain somewhat controversial. More recently it was shown for the Perseus Cluster that the energy resolutions of the CCD-type spectrometers on XMM-Newton and Chandra are not sufficient to uniquely and robustly distinguish between spectral distortions due to RS, different metal abundance profiles, and/or levels of gas turbulence (Zhuravleva et al. [2013](#)).

Here we present Hitomi observations of the RS effect in the core of the Perseus Cluster. Due to the superb energy resolution (full width at half maximum ∼5 eV at 6 keV) of the non-dispersive Soft X-ray Spectrometer (SXS) on board Hitomi, individual spectral lines are resolved (Hitomi Collaboration [2016](#)), allowing us to measure the suppression of

the flux in the He-like Fe $n = 1$–2 resonance line at 6.7 keV for the first time. As we discuss below, this suppression is likely due to photons having been scattered out of the line of sight.

Given that the optical depth at the center of a line depends on the turbulent Doppler broadening, the comparison of fluxes for optically thin and thick lines can be used to measure the characteristic amplitude of gas velocities in the ICM, complementing direct velocity measurements via Doppler broadening and centroid shifts. The RS technique has previously been successfully applied to high-resolution spectra from the cool ($kT \sim 1\,\mathrm{keV}$), dense cores of massive elliptical galaxies and galaxy groups, using deep XMM-Newton observations with the Reflection Grating Spectrometer (RGS). Detailed study of those data showed that the Fe XVII resonance line at 15.01 Å is suppressed in the dense galaxy cores, but not in the surrounding regions, while the line at 17.05 Å from the same ion is optically thin and is not suppressed (e.g., Xu et al. 2002; Kahn et al. 2003; Hayashi et al. 2009; Pinto et al. 2016; Ahoranta et al. 2016). Performing modeling of the RS effect, accounting for different levels of turbulence, revealed random gas velocities of the order of $\sim 100\,\mathrm{km\,s^{-1}}$ in many elliptical galaxies and groups (e.g., Werner et al. 2009; de Plaa et al. 2012; Ogorzalek et al. 2017).

Doppler spectroscopy and the RS technique provide complementary, non-redundant constraints on the velocity field. A measurement of the Doppler broadening along a given line of sight depends on the line-of-sight integral of the velocity field weighted by the square of the density. In contrast, the RS effect probes the integral of the velocity field along photon trajectories, weighted by the density itself. Even more striking, if turbulence is isotropic, the measurements of the Doppler effect and RS should provide the same results. If the measured velocities differ, this may indicate that the velocity field is anisotropic. Namely, if motions are radial (tangential) the scattering efficiency is reduced (increased) compared to the isotropic case (Zhuravleva et al. 2011). It is also important to note that the RS technique is mostly sensitive to small-scale motions (Zhuravleva et al. 2011). The comparison between the two measurements of the velocity field can also reveal large-scale deviations from spherical symmetry, and density inhomogeneities.

Hitomi Collaboration (2016) mentioned the presence of the RS effect in the Perseus core. The measured ratio of the Fe XXV Heα resonance to forbidden line fluxes, 2.48 ± 0.16 with 90% statistical uncertainties, is smaller than the predicted ratio in optically thin plasma with a mean gas temperature of 3.8 keV. Hitomi Collaboration (2016) also reports velocity dispersions of 187 ± 13 and $164 \pm 10\,\mathrm{km\,s^{-1}}$ in the core and outer regions, respectively. Theoretical studies of

the RS effect predict that the resonance line flux should still be suppressed if gas is moving with such velocities in the Perseus Cluster. In this paper, we measure spatial variations of line ratios and widths using the improved calibration data and taking systematic uncertainties into account. We confirm the presence of the RS effect and, using numerical simulations of radiative transfer in the Perseus Cluster, infer the velocities of gas motions. We refer the reader to Hitomi Collaboration (2017, 2018a, 2018b, 2018c) for the most complete analysis of spectroscopic velocity measurements, details of the plasma modeling, and detailed measurements of the temperature structure.[1] The ICM parameters presented in this paper are consistent with the measurements in these papers; small variations of specific parameters do not affect our conclusions.

The structure of our paper is as follows. In section 2, we describe the observations and data reduction. In section 3, we demonstrate that the complex coupled spectral and spatial behavior of the emission line intensities in the Fe XXV Heα spectrum are qualitatively consistent with the presence of RS. In section 4, we measure line intensity ratios that are sensitive to RS, as a function of position in the cluster. In section 5, we describe the radiative transfer simulations performed. We used two independent simulation codes: one based on the software packages of the `Geant4` tool kit[2] and HEAsim,[3] and one custom-written by one of us (IZ) based on Sazonov, Churazov, and Sunyaev (2002); we will refer to this latter code as the ICM Monte Carlo code or "ICMMC code." In section 6, we compare the results of simulations with the measured line ratios, and derive constraints on the turbulent velocity field. In section 7, we discuss the uncertainties associated with the atomic excitation rates, and possible presence of additional excitation processes such as charge exchange. The results are summarized and discussed in section 8.

Throughout this paper we adopt AtomDB version 3.0.8,[4] and the plasma emission models in APEC.[5] All data analysis software tasks refer to the HEAsoft package.[6] We adopt a Galactic hydrogen column density of $N_{\mathrm{H}} = 1.38 \times 10^{21}\,\mathrm{cm^{-2}}$ (Kalberla et al. 2005) in the direction of the Perseus Cluster, and use the solar abundance table provided by Lodders and Palme (2009). Unless noted otherwise, the errors are the 68% ($1\,\sigma$) confidence limits for a single parameter of interest.

---

[1] We will refer these papers as the "Atomic" or "A," the "Velocity" or "V," the "Temperature" or "T," and the "Abundance" or "Z," respectively.

[2] ⟨http://geant4.cern.ch⟩.

[3] ⟨https://heasarc.gsfc.nasa.gov/ftools/caldb/help/heasim.html⟩.

[4] ⟨http://www.atomdb.org⟩.

[5] Astrophysical Plasma Emission Code ⟨http://www.atomdb.org⟩.

[6] ⟨https://heasarc.nasa.gov/lheasoft⟩.

Table 1. Hitomi observations of the Perseus Cluster.

Region ID	Seq. no.	Obs. date	(RA, Dec)* (J2000.0)	Exp.[†] (ks)
obs. 1	100040010	2016-02-24T02:19:41	$(3^h19^m29^s.8, +41°29'1''.9)$	48.7
obs. 2	100040020	2016-02-25T02:14:13	$(3^h19^m43^s.6, +41°31'9''.8)$	97.4
obs. 3	100040030/100040040/100040050	2016-03-04T02:17:32	$(3^h19^m43^s.8, +41°31'12''.5)$	146.1
obs. 4	100040060	2016-03-06T22:56:20	$(3^h19^m48^s.2, +41°30'44''.1)$	45.8

*Average pointing direction of the Hitomi SXS, as recorded in the RA_NOM and DEC_NOM keywords of the event FITS files.

[†]After screening on rise time cut and for events that occur near in time to other events.
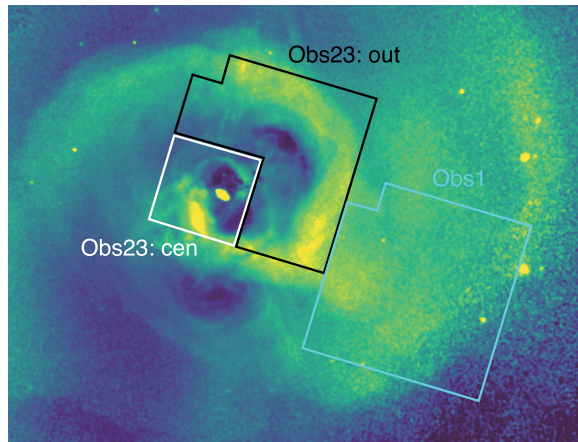
Fig. 1. Hitomi SXS observation regions overlaid on the Chandra X-ray image of the Perseus Cluster in the 1.8–9.0 keV band divided by the spherically symmetric model for the surface brightness. In this paper we will consider obs23_cen as the central region, which includes the central AGN (white), outer region obs23_out (black), and obs1_whole (cyan). (Color online)

2 Observation and data reduction

Hitomi carried out a series of four overlapping pointed observations of the Perseus Cluster core during its commissioning phase in 2016 February and March, with a total of 340 ks exposure time (see table 1 and figure 1). The Hitomi SXS is a system that combines an X-ray micro-calorimeter spectrometer with a Soft X-ray Telescope (SXT) to cover a $3' \times 3'$ field of view (FOV) with an angular resolution of $1'.2$ (half power diameter). The micro-calorimeter spectrometer provided a spectral energy resolution of $\Delta E \sim 5$ eV at 6 keV (Kelley et al. 2016). It is operated inside a dewar, in which a multi-stage cooling system maintains a stable environment at 50 mK; temperature stability is important to give such a high energy resolution. The SXS was originally expected to cover the energy range between 0.3 and 12 keV, but only data in the $E \gtrsim 2$ keV band were available during the Perseus observations because the gate valve on the SXS dewar, which consists of a Be window and its support structure, was still closed at the time of observation. The other instruments on Hitomi are described in

Takahashi et al. (2017). In this paper, we use only the SXS data for investigating RS in the Perseus Cluster core.

The Perseus Cluster was observed four times with Hitomi over a 10 d period, but the SXS dewar had not yet achieved thermal equilibrium during the first two observations. A drift in temperature of the detector implies a drift in the photon energy to signal conversion (the so-called "gain"). For the observations during which the gain drift was significant, the photon energy scale was determined using the data processing routine "sxsperseus" in HEAsoft, which corrects the gain scale via an extrapolation of the relationship between the relative gain changes on the array and on the continuously illuminated calibration pixel from the Perseus observation to the later full-array calibration in the official data pipeline processing. Observations 1 and 2 in table 1 were affected by this gain drift; observations 3 and 4 were obtained under thermal equilibrium in the SXS dewar. A difference in gain between obs. 2, and the sum of obs. 3 and 4 (full FOV) of ~2 eV can still be seen (M. E. Eckart et al. in preparation). It is most clearly seen around the Fe XXV Heα line complex in the official data pipeline processing (Angelini et al. 2016). Not surprisingly, obs. 1 has a much larger energy scale uncertainty (Porter et al. 2016). All pixels in the micro-calorimeter array are independent, and in principle each has its own energy scale, and energy scale variations.

In our spectral analysis of the central region in section 4 we have to take the contribution of non-thermal emission from the central AGN in the Perseus Cluster, NGC 1275, explicitly into account. Following the "T" paper, we applied the "sxsextend" task to register event energies above 16 keV, so that we can construct the spectrum up to ~20 keV. This is crucial to discriminate the AGN and cluster gas components spectrally, as the former dominates the spectrum in the extended energy band. This method is same as that in the "T" paper (Hitomi Collaboration 2018b). After having added the high-energy events, and having applied the extra screenings, we adopted two extra gain corrections, similar to the procedures described in the "A" paper (Hitomi Collaboration 2018c), but used a different reference redshift of 0.017284 according to the

"V" paper (Hitomi Collaboration 2018a). The detailed correction parameters were shown in the appendix to the "T" paper (Hitomi Collaboration 2018b). The first of these corrections is referred to as the "z-correction," which adjusts the absolute energy scale of each pixel in each data set such that the redshift of the Fe XXV Heα resonance line is aligned to the redshift of NGC 1275 at $z = 0.017284$. The second is referred to as the "quadratic-curve-correction," which applies a second-order correction, centered on Fe XXV Heα, to take out small apparent offsets in the observed energies of the strongest emission lines across the 1.8–9 keV band. The intent of the "z-correction" is to allow the spectra from different pixels and different pointings to be added with minimal broadening of the lines from variation in the bulk velocity across the Perseus Cluster within the SXS FOV. For the RS analysis we need to measure the ratios of line fluxes, thus we use the full available data set to reduce statistical uncertainties on measured line ratios, presuming variations across the data set are sufficiently small to warrant this approach. The uncertainties in the RS analysis associated with the energy scale corrections are discussed in section 4.

After applying all these corrections, the spectra were extracted with the Xselect package in HEAsoft for each region as shown in figure 2. We used only high primary grade event data to generate the spectra. In order to subtract the non-X-ray background (NXB), we employed the day and dark Earth database using the "sxsnxbgen" Ftools task. We generated a redistribution matrix file (RMF) including the escape peak and electron loss continuum effects with the "`whichrmf=x`" option in the "sxsmkrmf" task to represent the spectral shape in the lower and higher energy bands. Because the spatial distributions of the ICM and AGN components are different, we also made two kinds of ancillary response files (ARFs) for the spectrum of each region, A^P and A^C. The response A^P assumed point-like source emission from NGC 1275 centered on (RA, Dec) = ($3^h19^m48^s1$, $+41°30'42''$); A^C is appropriate to the diffuse emission from the ICM, and is based on the X-ray image observed with Chandra in the 1.8–9.0 keV energy band, with a region of radius $10''$ centered on the AGN replaced with the average surrounding brightness by the "aharfgen" task in HEAsoft. At the time operations ceased, a full in-orbit calibration of the spatial response and effective area had not yet been performed well. In this paper, we therefore use ARFs generated based on the ground calibration of SXT. A "fudge factor" was derived from the ground measurements, to adjust the calibration to in-flight performance; however, this fudge factor has large uncertainties, as shown in Tsujimoto et al. (2017) and Hitomi Collaboration (2018b), and the spectral fits with these "fudged" ARFs produced artificial residual features. We also examined an adjustment of the "Crab ratio" using the

Crab observation with Hitomi SXS (Tsujimoto et al. 2017); however, this adjustment also introduced systematic residuals around the Au and Hg edges around 12 keV, as shown in the "T" paper (Hitomi Collaboration 2018b). We therefore decided not to apply such corrections and use the standard ground-calibration-based response. Finally, in all spectral fits, the spectra are grouped with 1 eV bin^{-1}, and 1 count per bin at least, allowing the C-statistics method to be used.

We extracted spectra from three regions, obs23_cen and obs23_out from obs. 2 and 3, and obs1_whole from obs. 1, with the region boundaries coinciding with detector pixel boundaries as shown in figure 1, in order to avoid having to redistribute photons between pixels. The pointing directions of obs. 2 and 3 are slightly different (offset by $\sim$0$'$1); however, this offset is much smaller than the size of the SXS point spread function. The obs23_cen, obs23_out, and obs1_whole regions are located on the central 9 pixels around the AGN, the outer 26 pixels of obs. 2 and 3, and the whole region of obs. 1, respectively— see figure 1. The observed spectra in the 6.1–7.9 keV band are shown in figure 2. Their modeling is discussed below in section 4.

3 Observational indications for resonant scattering

Theoretical studies of the RS effect in the Perseus Cluster predict that, in the absence of gas motions, the degree of flux suppression in the resonance line of He-like Fe should vary with the projected distance from the cluster center: the line flux will be most suppressed in the innermost region, with the suppression decreasing with projected distance out to a radius of $\sim$100 kpc. At larger radii, the line flux is slightly increased relative to the value for the optically thin case (e.g., Churazov et al. 2004). Also, as the result of scattering, the wings of the line become slightly stronger (see, e.g., Zhuravleva et al. 2013). Below we demonstrate that the Perseus Hitomi data show evidence for both of these effects.

3.1 Flux suppression in the Fe XXV Heα resonance line

We first consider the spectrum of the He-like Fe XXV triplet from the innermost region (obs23_cen in figure 1), where the suppression of the resonance (w) line is expected to be the strongest. A single-temperature *bapec*[7] model for an optically thin plasma can approximately model the resonance line flux, but will then underestimate the fluxes of the neighboring forbidden (z) and intercombination (y)

---

[7] The *bapec* model describes a plasma in collisional ionization equilibrium, with arbitrary velocity broadening in addition to thermal Doppler broadening, and element abundance ratios relative to He fixed to the solar ratios.
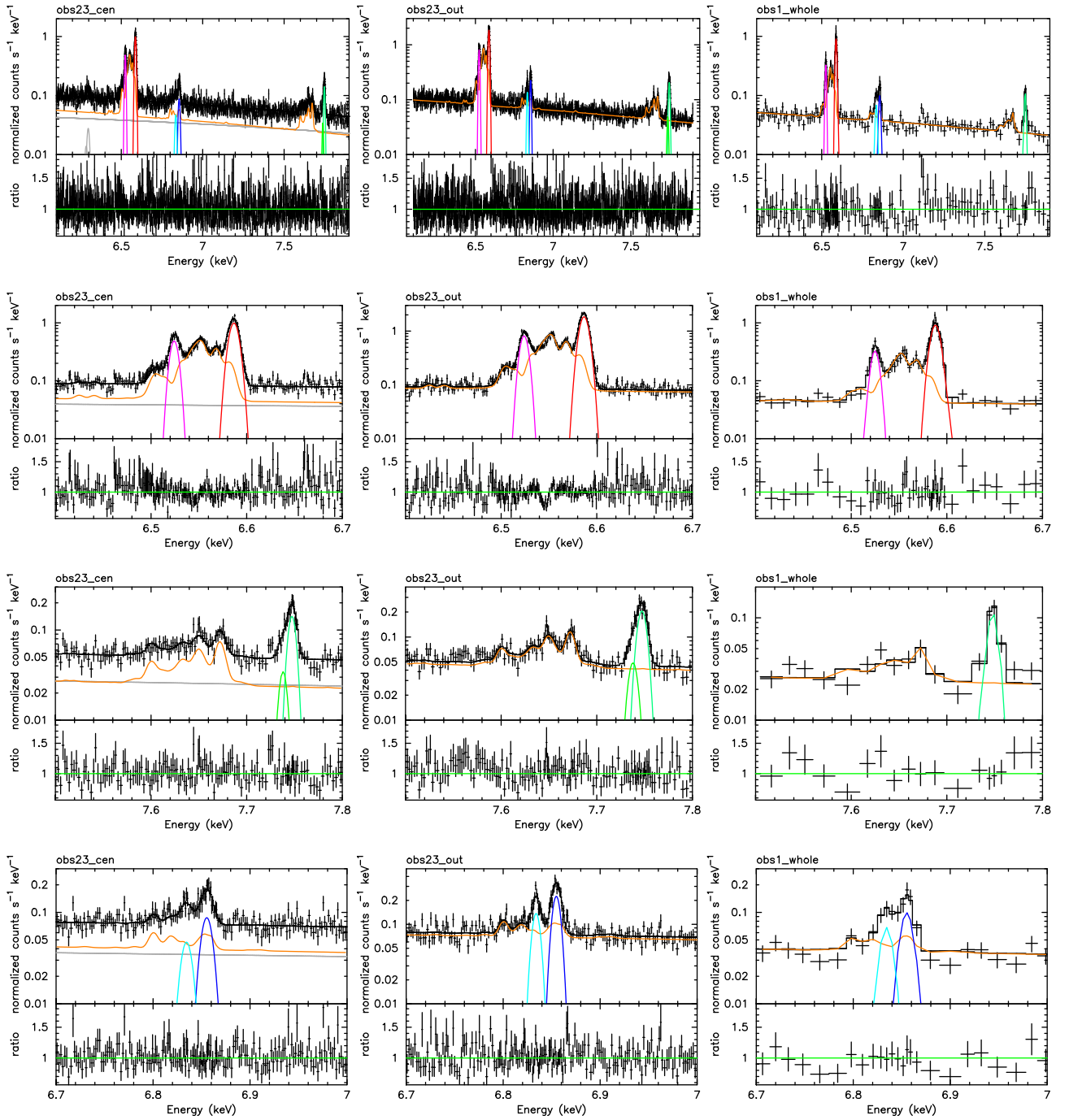
Fig. 2. Observed Hitomi spectra extracted from the obs23_cen, obs23_out, and obs1_whole regions shown in figure 1, and binned for display purposes. The top panels show the resultant spectral fits in the 6.1–7.9 keV band, while the second, third, and fourth rows show the energy range of the Heα complex lines in 6.4–6.7 keV, Heβ lines in 7.5–7.8 keV, and Lyα lines in 6.7–7 keV. The spectra obtained with the Hitomi SXS are shown in black; light gray lines show the emission from the AGN. Orange lines indicate the "modified" *bvvapec* model, in which the strongest lines have been deleted. The Fe XXV Heα forbidden and resonance, He$\beta_{1,2}$, and Fe XXVI Ly$\alpha_{1,2}$ are shown in magenta, red, green, light green, blue, and cyan lines, respectively. The lower panels show the fit residuals in units of ratio. (Color online)

lines (see bottom left panel of figure 3 and supplementary material in Hitomi Collaboration 2016). Exclusion of the resonance line from the modeling provides a better fit for *x*, *y*, and *z* and other weaker lines, but clearly overestimates the *w* flux (top left panel of figure 3). We then add a

Gaussian component to the model with the energy of the *w* line and normalization that is allowed to be negative. The best-fitting result of this model is shown in the top right panel of figure 3. The best-fitting normalization of the Gaussian component is indeed negative, and the model
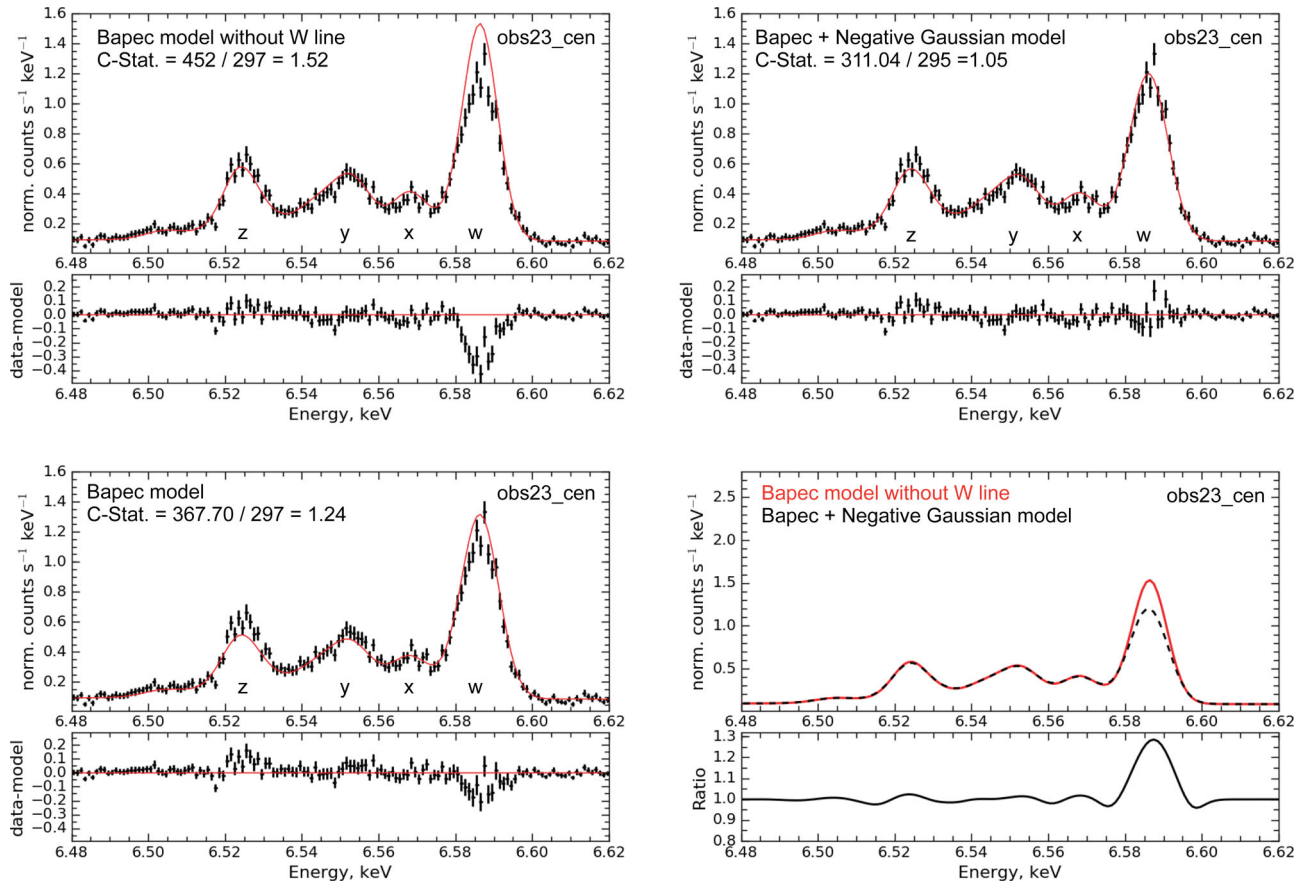
Fig. 3. Flux suppression in the strongest line of He-like Fe xxv (*w*) in the Perseus Cluster observed in the obs23_cen region. Black points show the Hitomi data; red lines in the corresponding panels show the best-fitting models. Top left: the spectrum is fitted with the *bapec* model, excluding the *w* line from the data; top right: the same spectrum is fitted with the *bapec* model and a Gaussian component centered at the energy of the *w* line—the normalization of the Gaussian model is allowed to be negative; bottom left: the same spectrum fitted with the *bapec* model. The comparison of the models from the top left (solid) and right (dashed) panels is shown in the bottom right panel. The suppression of the *w* line indicates the presence of the resonant scattering effect in the Perseus Cluster. See subsection 3.1 for details. (Color online)

provides a statistically better fit to the data than a pure *bapec* model.[8] The ratio of the best-fitting models shown in the top panels shows a suppression of the resonance line by a factor of ∼1.28, indicating the presence of RS.

The same modeling procedure is applied to spectra from the regions at larger distances from the cluster center (obs23_out and obs1_whole; see figure 1). When fitting the obs23_out spectrum, the *bapec+negative Gaussian* model provides a statistically better fit than the pure *bapec* model. The *w* flux in the obs23_out region is suppressed by factor of ∼1.28 (left panel of figure 4). In the region most distant from the cluster center, obs1_whole, the *bapec+negative Gaussian* model does not provide a statistically better fit of the data than a *bapec* model. The measured line suppression is small, less than 1.15 (right panel of figure 4). These simple experiments illustrate the possible presence of the RS effect in the Perseus core.

[8] For all three modeling steps we use the same gas temperature, which is taken from the best-fitting model to the data without the *w* line.

3.2 The broadening of the Fe xxv He α resonance line

In addition to flux suppression in the resonance line, the RS broadens the wings of the line. Even though the effect is significantly smaller than the line suppression, we have checked for indications of line broadening in the *w* line compared to other lines in the triplet. We fit the observed data excluding the *w* line with a single-temperature *bapec* model, from which the *w* line has been removed. Freezing the best-fitting parameters of this model, we fit the whole triplet, with the *w* line restored, adding an additional Gaussian component with the central energy of the *w* line. Such modeling allows us to measure the broadening of the *w* line independently from the broadening of other lines in the triplet. Accounting for statistical uncertainties, the turbulent broadening of the *w* line varies between 171 and 183 km s^{-1}, while the broadening of the *x*, *y*, and *z* lines is smaller: 145–165 km s^{-1}. A similar difference is observed in the obs23_out region. Namely, the *w* line turbulent
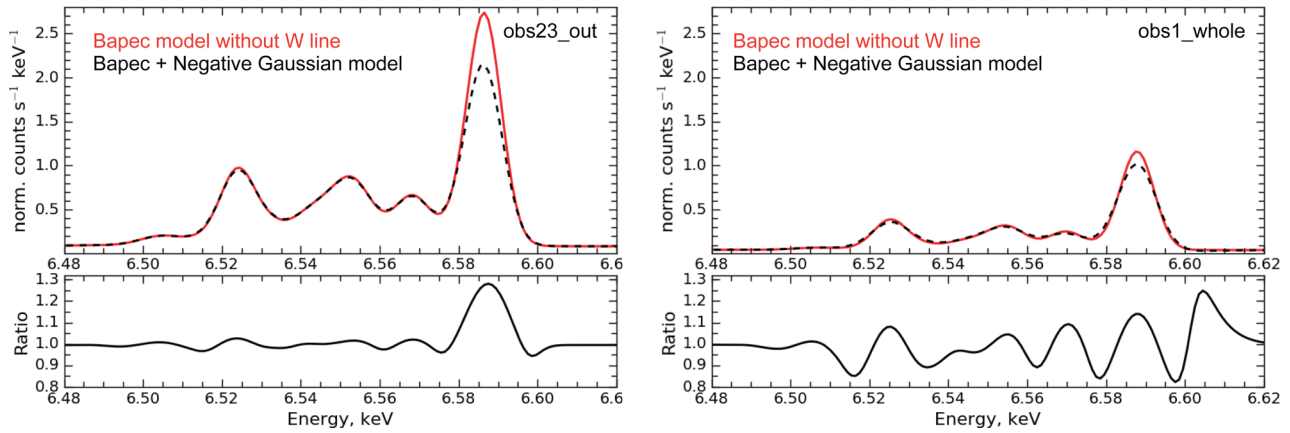
Fig. 4. Same as the bottom right panel in figure 3, but for the spectra observed in the obs23_out (left) and obs1_whole (right) regions. See subsection 3.1 for details. (Color online)

broadening in this region is 159–167 km s^{-1}, while in all other lines it is 136–150 km s^{-1}.

4 Observed line ratios

We fitted the spectra with a combination of emission models representing the AGN and the ICM, each with its own response, in Xspec. The AGN is represented by a power law with redshifted absorption, with additional (redshifted) Fe K$\alpha_{1,2}$ fluorescent emission lines; the ICM is modeled with a redshifted collisional ionization equilibrium plasma, with adjustable elemental abundances, and additional Gaussian emission lines if necessary. The two components share a common foreground neutral Galactic absorption. Formally, we have AGN model: $TBabs_{\rm GAL} \times (pegpwrlw_{\rm AGN} + zgauss_{\rm AGN, Fe\ K\alpha_1} + zgauss_{\rm AGN, Fe\ K\alpha_2})$; ICM model: $TBabs_{\rm GAL} \times (bvvapec_{\rm ICM} + zgauss_{\rm Fe\ lines})$. The AGN parameters are fixed at the numbers in the NGC 1275 paper (Hitomi Collaboration 2018d). In this paper we modify the $bvvapec$ model, setting the emissivities of the strong Fe lines to zero.

First, we derived the ICM temperature, Fe abundance, turbulent velocity, and normalizations from the spectral fits in 1.8–20.0 keV with a single-temperature model for each region. In the broad-band fit, to determine those parameters, we adopted the modified $bvvapec$ model, from which the Fe XXV Heα resonance line is excluded, and the corresponding Gaussian model is added. The resultant parameters and C-statistics from the spectral fits for each region are shown in table 2. The "projected" temperature increases slightly with radius, while the Fe abundance drops by ∼0.1 solar from the center to the obs1_whole region. The measured temperature and Fe abundance gradients agree with the results from the "T" and "Z" papers (Hitomi Collaboration 2017, 2018b). As for the turbulent velocity, $\sigma_{\rm v}$, the

derived values are almost constant with radius. These $\sigma_{\rm v}$ in the previous Hitomi paper (Hitomi Collaboration 2016) and "V" paper (Hitomi Collaboration 2018a) are slightly different. We note that the data reduction, calibrations, and plasma codes are improved over the previous Hitomi paper. Also, the numbers shown in table 4 for PSF uncorrected in the "V" paper from their narrow-band fits in the 6.4–6.7 keV band are slightly smaller than those from the broad-band fits shown in table 2 in this paper. The difference comes from the broader line width of the Lyα lines (see table 2 and the "V" paper).

Fixing the ICM temperature, Fe abundance, and $\sigma_{\rm v}$ at the values from the broad-band fits, we exclude the Fe XXV Heα forbidden (z) and resonance (w), the Heβ, and the Fe XXVI Lyα lines from the $bvvapec$ model and include Gaussian line models instead with the central energies of these lines. The best-fitting normalizations of the Gaussian components give the total fluxes of these lines. Here, the line widths of the Lyα_2 and Heβ_2 are linked to the Lyα_1 and Heβ_1 lines, respectively, and other parameters except for the redshift are varied in the spectral fits. This fitting model is very useful since $bvvapec$ describes the weak satellite lines, while the added Gaussian lines allow us to measure the fluxes of the strongest emission lines in a model-independent way, taking blending with weaker emission lines into account.

The observed spectra are described well by the model, except around the 6.55 keV feature, as shown in figure 2. The resulting line ratios and widths (thermal and turbulent broadenings, $\sigma_{\rm v+th}$) are summarized in table 2 and figure 5. The Lyα_1 and Lyα_2 lines are clearly resolved in the obs23_cen and obs23_out regions, while the Heβ lines are not, due to their close central energies. Note that the emission lines are represented well by the corresponding Gaussian models, as confirmed by the study of possible non-Gaussianity in the "V" paper. The derived radial profile of

Table 2. Summary of the best-fit properties of temperatures, Fe abundance, turbulent velocity (σ_v), C-statistics, line ratios, and line widths (σ_{v+th}).

Region ID	kT* (keV)	Fe* (solar)	σ_v* (km s^{-1})	C-stat/d.o.f.* (1.8–20 keV)	C-stat/d.o.f.† (6.1–7.9 keV)		
obs23_cen	3.92 ± 0.03	0.65 ± 0.01	155 ± 7	10609/11151	1793/1784		
obs23_out	4.05 ± 0.01	0.65 ± 0.01	141 ± 5	14559/11744	1964/1784		
obs1_whole	5.06 ± 0.07	0.53 ± 0.02	159 ± 17	6333/6930	1283/1494		
Region ID Line ratio	$w/z^\dagger$	$w/\mathrm{He}\beta^\dagger$	$w/\mathrm{Ly}\alpha_1^\dagger$	$w/\mathrm{Ly}\alpha_2^\dagger$	$z/\mathrm{He}\beta^\dagger$	$z/\mathrm{Ly}\alpha_1^\dagger$	$z/\mathrm{Ly}\alpha_2^\dagger$
obs23_cen	2.45 ± 0.11	5.98 ± 0.57	9.79 ± 0.98	18.17 ± 2.76	2.45 ± 0.25	4.00 ± 0.42	7.42 ± 0.36
obs23_out	2.59 ± 0.08	6.23 ± 0.57	9.36 ± 0.57	15.41 ± 1.24	2.40 ± 0.23	3.61 ± 0.24	5.95 ± 0.20
obs1_whole	3.27 ± 0.34	6.35 ± 0.95	6.87 ± 1.11	9.80 ± 1.96	1.94 ± 0.33	2.10 ± 0.38	3.00 ± 0.35
Region ID Line width (σ_{v+th})	$w^\dagger$ (eV)	$z^\dagger$ (eV)	$\mathrm{Ly}\alpha^\dagger$ (eV)	$\mathrm{He}\beta^\dagger$ (eV)			
obs23_cen	4.49 ± 0.11	3.57 ± 0.21	5.29 ± 0.55	3.45 ± 0.50			
obs23_out	4.20 ± 0.08	3.54 ± 0.15	3.46 ± 0.25	4.24 ± 0.42			
obs1_whole	4.43 ± 0.24	3.58 ± 0.50	6.09 ± 0.89	4.81 ± 0.80			

*Fits in the broad 1.8–20.0 keV band with the AGN and modified *bvvapec* models, from which the resonance line is excluded and a Gaussian component is added instead. σ_v is a turbulent velocity in the *bvvapec* model without the resonance line. The numbers in this table are slightly smaller than those in the "V" paper (Hitomi Collaboration 2018a); see section 4 for the details.

†Fits in the narrow, 6.1–7.9 keV, band with the AGN and modified *bvvapec* models, from which we exclude the Heα resonance and forbidden, Heβ1&2, and Lyα1&2 lines.

the w/z ratio increases with the distance from the center, while the $z/\mathrm{He}\beta$ ratio is almost the same everywhere. The measured w line widths in the obs23_cen and obs23_out regions are broader than the z ones at the $\sim 2\sigma$ level. The comparison of the measured line ratios and line broadening with the results of numerical simulations of the RS effect is discussed in section 5.

Systematic uncertainties, such as (i) the ICM modeling of a single or two temperature structure, (ii) gain correction, (iii) the point spread function (PSF) deblending, and (iv) plasma codes (AtomDB version 3.0.8 or 3.0.9) should be considered in the spectral analysis. Estimates of their effects are examined below. As a result, these uncertainties almost do not affect our results and conclusions.

As for the ICM modeling, the Fe lines in the 6–8 keV band are modeled well with a single-temperature (1T) model with the exception of the resonance (w) line shown in figure 2 and table 2. On the other hand, as described in the "T" paper, a two-temperature (2T) model improves the spectral fits when the AtomDB version is 3.0.9. The w/z ratios measured from the 1T and 2T models agree within the statistical error with either AtomDB version 3.0.8 or 3.0.9. In this paper, since we examined the spectral fits for the observations and simulations in the same manner, i.e., the same model formula, as described in subsection 5.3, and compare the resultant fit parameters, the choice of the 1T or 2T models does not affect our conclusions, as long as the continuum spectra are well-represented by the

models. Note that the gas temperature measured from the line ratios obtained from the 2T model in the "T" paper agree well with the deprojected temperature profile from the Chandra data.

We repeated the spectral analysis using gain-uncorrected Hitomi data to estimate the uncertainty. Figure 6 shows comparison plots of the resultant fits for the w/z and $z/\mathrm{He}\beta$ line ratios and line widths, σ_{v+th}, of the w and z lines between the gain-corrected and uncorrected data. The line ratios from both data sets are consistent within the statistical errors. At the same time, the width of the w line in obs23_cen decreases, as expected, by about 5% when the gain correction is applied. We did not correct the spectral fit for the PSF effects. The azimuth-averaged values in regions 1–4 for the PSF uncorrected numbers in the "V" paper, which roughly correspond to the obs23_out region, are almost consistent with our results within statistical errors. The PSF effect is accounted for in the simulations in this paper described in section 5. The residuals around 6.55 keV in the obs23_out region are likely associated with uncertainties in the plasma model for the Fe XXIV Li-like line (see also figure 8 in the "Atomic" paper). These come from underestimation of the Li-like lines in AtomDB version 3.0.8. The updated version 3.0.9 corrected for the problem, as shown in the Appendix. This feature has negligible impact on our results for line ratios and widths, however, since the Li-like lines are separated from the w and z lines.
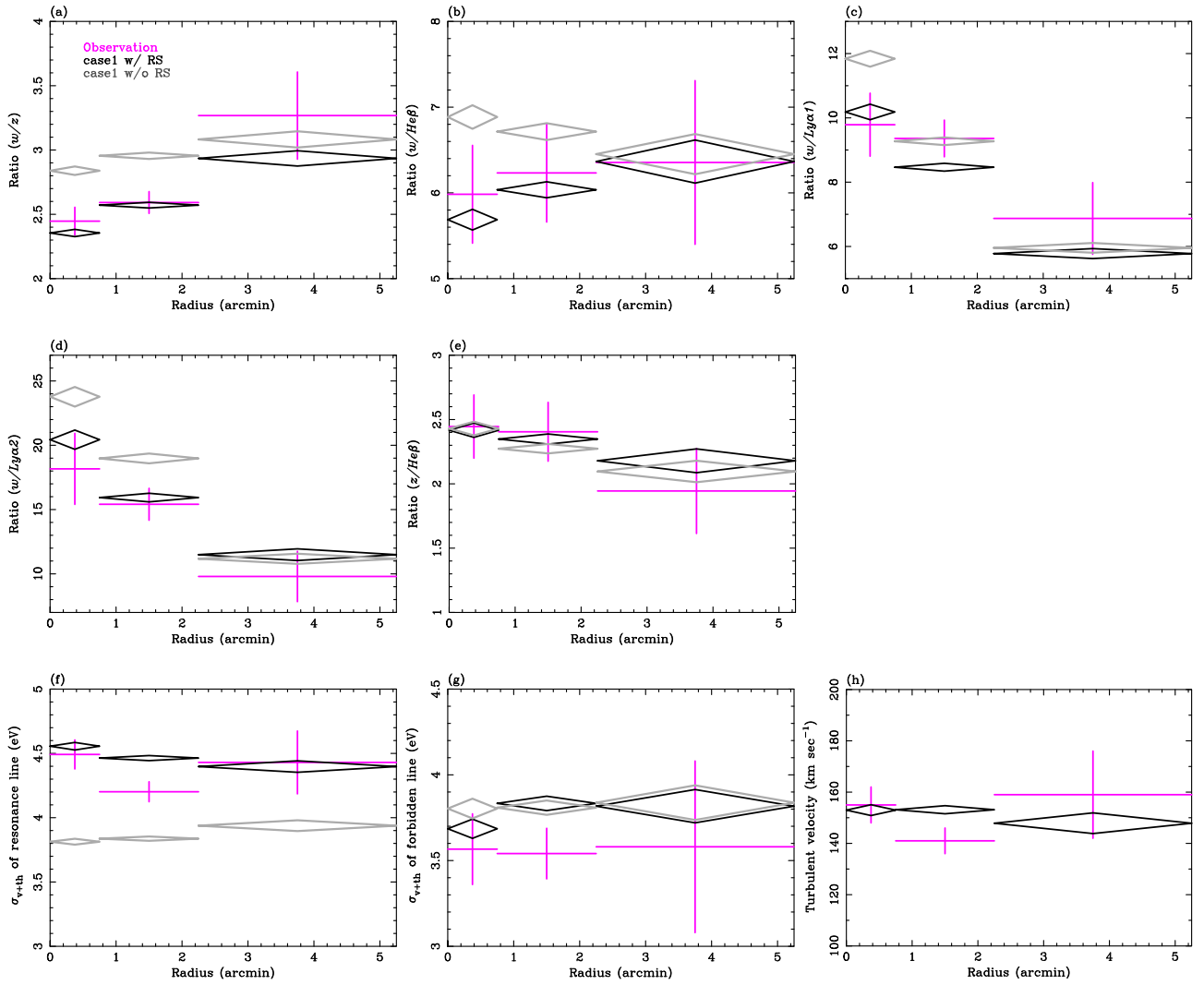
Fig. 5. (a)–(e): Comparisons of the observed and predicted ratios of the Fe Heα resonance (*w*), Heα forbidden (*z*), Heβ, and Lyα$_{1,2}$ lines. Observations are shown as magenta crosses and the simulations with RS as black diamonds, and the same without RS as gray diamonds for the assumption of a constant σ_v of 150 km s^{-1} (case 1). (f)–(g): Comparisons of the widths of the resonance (*w*) and forbidden (*z*) lines between observation (magenta crosses) and simulations with RS (black diamonds) and without RS (gray diamonds). (h): Comparisons of the derived turbulent velocities from the spectral fits between observation (magenta cross) in broad-band fits and the simulations. (Color online)

5 Radiative transfer simulations

The line suppression due to the RS effect is sensitive to the velocity of gas motions: the larger the velocity of gas motions the lower the probability of scattering and the closer the line ratios to those for an optically thin plasma. In order to interpret the observed line suppression and infer the velocity of gas motions, we performed radiative transfer Monte Carlo (MC) simulations of the RS in the Perseus Cluster. We followed two independent approaches: (i) using the `Geant4` and HEAsim tools and assuming a velocity field consistent with the direct velocity measurements as presented in the "V" paper (Hitomi Collaboration 2018a), and (ii) using a proprietary code written specifically for MC simulations of radiative transfer in the cluster ICM (ICMMC).

Both approaches are based on the emission models for an optically thin plasma taken from AtomDB version 3.0.8, and take into account projection effects (gas density, temperature, abundance of heavy elements) and the spatial response of the telescope. The latter is treated differently in the two approaches. The results based on both simulations broadly agree. Details of the two approaches are discussed below.

5.1 Model of the Perseus Cluster

For the MC simulations, we adopt a spherically symmetric model of the Perseus Cluster. We used archival Chandra data to measure the profiles of gas density, temperature,
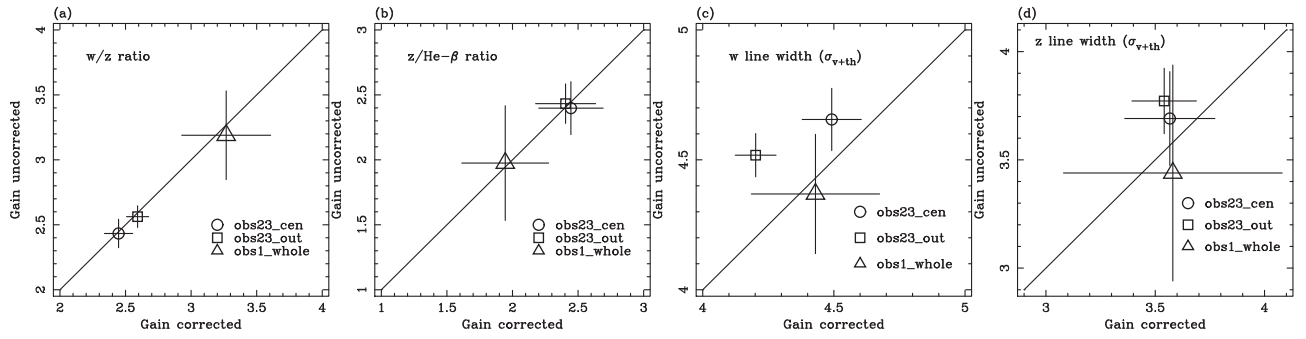
Fig. 6. Scattering plots between the gain-corrected and uncorrected data for (a) the w/z line ratio, (b) the $z/\mathrm{He}\beta$ line ratio, (c) w line width ($\sigma_{\mathrm{v+th}}$), and (d) z line width ($\sigma_{\mathrm{v+th}}$). The open circles, squares, and triangles correspond to the measurements in the obs23_cen, obs23_out, and obs1_whole regions, respectively.
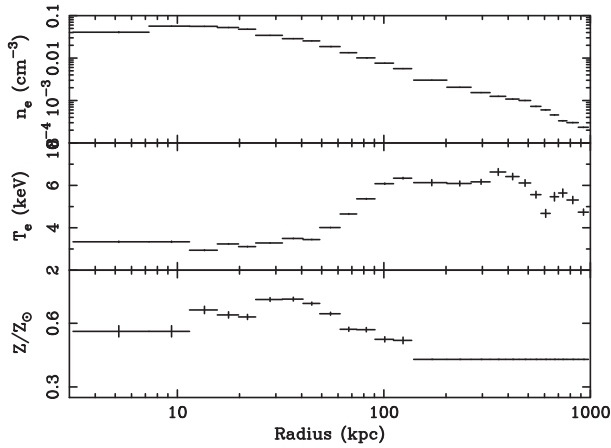

Fig. 7. Model of the Perseus Cluster used for the Monte Carlo simulations of radiative transfer in strong emission lines. Top: deprojected electron number density; middle: deprojected gas electron temperature; bottom: deprojected abundance of heavy elements relative to solar abundance from Lodders and Palme (2009). Chandra data are used in the inner ~150 kpc region. These profiles of the temperature and electron density are merged with Suzaku deprojected data at large radii, $r \gtrsim 150$ kpc, taken from Urban et al. (2014), and the abundance is adopted to be the averaged number in Werner et al. (2013), Matsushita et al. (2013), and Urban et al. (2014).

and abundance of heavy elements. Excluding point sources and the central AGN, projected spectra are obtained in radial annuli, centered on the central galaxy, NGC 1275. These are deprojected following the procedure described by Churazov et al. (2003). The spectra are fitted with an *apec* model in a broad energy band, 0.5–8.5 keV, accounting for Galactic foreground absorption by a column density of $N_{\mathrm{H}} = 1.38 \times 10^{21}\,\mathrm{cm}^{-2}$, and treating the abundance of heavy elements as a free parameter, using the solar abundance table by Lodders and Palme (2009). The Chandra deprojected profile within ~150 kpc is shown in figure 7. There is a density drop in the innermost region (the first point from the center) likely associated with the bubbles of relativistic plasma that push up the X-ray gas. Due to this

density drop and the presence of multi-temperature plasma, the deprojected temperature and the heavy element abundances are not determined reliably in this region. Therefore, we assume constant temperature and abundance profiles in the inner ~10 kpc region. The Chandra deprojected profile is then merged with the Suzaku deprojected data (Urban et al. 2014) at large radii, $r > 150$ kpc. As for the abundances in $r = 150$–1000 kpc, since the observed abundances (~0.3 solar) from Suzaku in Werner et al. (2013) and Urban et al. (2014) are relatively smaller than those (~0.5 solar) from XMM in Matsushita et al. (2013), we adopted the averaged number of ~0.4 solar as the input parameter. Figure 7 shows the combined radial profiles.

5.2 Optical depth

Using the equations shown in Zhuravleva et al. (2013), the optical depth is calculated from the center of the cluster out to a radius corresponding to an angular size on the sky of $40' \sim 830$ kpc, corresponding to 2/3 times r_{500} (Urban et al. 2014). The left panel of figure 8 shows the optical depth for each line (see also table 3) for the case of zero σ_{v} calculated using the cluster model described in subsection 5.1. Resonant scattering is expected to be important in the central regions of the Perseus Cluster, where the optical depth is larger than 1. The Fe XXV Heα w has the largest optical depth, ~2.3, while the Fe XXV Heα z line is essentially optically thin and not affected by the RS.

The optical depth is inversely proportional to the Doppler line width, which depends on the thermal broadening and turbulent gas motions. Therefore, the stronger the turbulence, the smaller the optical depth (see figure 8, right panel). However, even if the gas is moving with a characteristic velocity as large as ~150–200 km s^{-1}, as measured directly through the line broadening, we still expect RS to affect the w line (the optical depth is ~1). All other lines considered in this work are effectively optically thin.
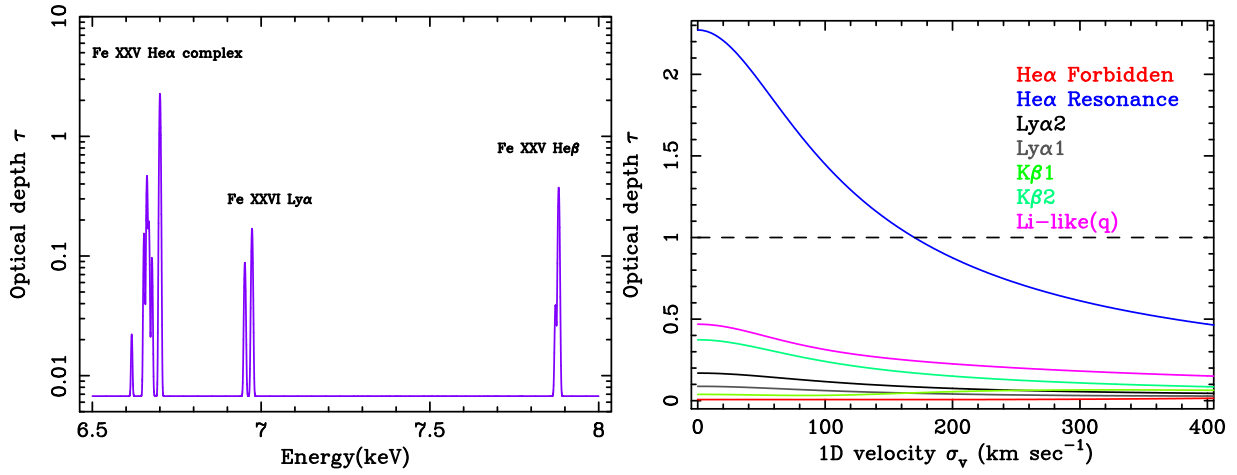
Fig. 8. Left: Optical depth in lines and continuum as a function of photon energy calculated assuming zero turbulent velocity and integrated over an $r = 0'–40'$ region (see also table 3). Right: Optical depth profile of the Fe XXIV, XXV, XXVI lines vs. the velocity of gas motions in units of km s^{-1}. (Color online)

Table 3. Rest-frame Fe line properties in the 6–8 keV band that have optical depth $\gtrsim 0.01$.

Ion	Energy (eV)	Lower level*	Upper level*	Oscillator strength	Optical depth τ $\sigma_{\rm v} = 0\,{\rm km\,s^{-1}}$	Comments*
Fe XXIV	6616.73	$1s^2 2s_{1/2}\,{}^2S_{1/2}$	$1s_{1/2} 2s_{1/2} 2p_{1/2}\,{}^4P_{3/2}$	3.26×10^{-2}	2.22×10^{-2}	u
Fe XXV	6636.58	$1s^2\,{}^1S_0$	$1s2s\,{}^3S_1$	3.03×10^{-7}	6.75×10^{-3}	Heα, z
Fe XXIV	6653.30	$1s^2 2s_{1/2}\,{}^2S_{1/2}$	$1s_{1/2} 2s_{1/2} 2p_{1/2}\,{}^2P_{1/2}$	3.13×10^{-1}	1.54×10^{-2}	r
Fe XXIV	6661.88	$1s^2 2s_{1/2}\,{}^2S_{1/2}$	$1s_{1/2} 2s_{1/2} 2p_{3/2}\,{}^2P_{3/2}$	9.78×10^{-1}	4.69×10^{-1}	q
Fe XXV	6667.55	$1s^2\,{}^1S_0$	$1s_{1/2} 2p_{1/2}\,{}^3P_1$	5.79×10^{-2}	1.92×10^{-1}	Heα, y
Fe XXIV	6676.59	$1s^2 2s_{1/2}\,{}^2S_{1/2}$	$1s_{1/2} 2s_{1/2} 2p_{3/2}\,{}^2P_{1/2}$	1.92×10^{-1}	9.67×10^{-2}	t
Fe XXV	6682.30	$1s^2\,{}^1S_0$	$1s_{1/2} 2p_{3/2}\,{}^3P_2$	1.70×10^{-5}	7.26×10^{-3}	Heα, x
Fe XXV	6700.40	$1s^2\,{}^1S_0$	$1s_{1/2} 2p_{3/2}\,{}^1P_1$	7.19×10^{-1}	2.27	Heα, w
Fe XXVI	6951.86	$1s$	$2p_{1/2}$	1.36×10^{-1}	8.81×10^{-2}	Lyα_2
Fe XXVI	6973.07	$1s$	$2p_{3/2}$	2.73×10^{-1}	1.69×10^{-1}	Lyα_1
Fe XXV	7872.01	$1s^2\,{}^1S_0$	$1s3p\,{}^3P_1$	1.18×10^{-2}	3.87×10^{-2}	Heβ_2, intercomb.
Fe XXV	7881.52	$1s^2\,{}^1S_0$	$1s3p\,{}^1P_1$	1.37×10^{-1}	3.73×10^{-1}	Heβ_1, resonance

*Optical depths are integrated over an $r = 0'–40'$ region with $\sigma_{\rm v} = 0\,{\rm km\,s^{-1}}$. Energies and oscillator strengths are from AtomDB version 3.0.8.
†Letter designations for the transitions as per Gabriel (1972).

5.3 Monte Carlo simulations with Geant4

The RS simulation was performed with the main reaction processes shown in Zhuravleva et al. (2013), using the input Perseus model shown in figure 7. Assuming spherical symmetry, we calculated multiple scatterings of photons in the Perseus core; the Geant4 toolkit produces a list of simulated photons incident on the Hitomi SXS. In the Geant4 framework, we assume 400 spherical shells in an $r = 0'–40'$ region, and scaled to be 1 kpc = 1 cm to preserve the scattering probability under the low-density environment in the ICM. The seed photons in the simulator are generated according to the thermal emissivity associated with our adopted spatial distributions of density, temperature, and abundance, and we assume the photons are emitted isotropically. Scattering probabilities are calculated using the mean free path of each photon in each shell, assuming

thermally and turbulently broadened Fe line absorption, as well as Thomson scattering, including a proper energy transfer and scattering direction of the incident photons after RS in the cluster and ion velocity field, which are uniquely implemented in Geant4. The Fe line emissivity and oscillator strength are taken from AtomDB version 3.0.8. In the simulation, we include scattering by the set of the Fe XXIV, XXV, XXVI lines shown in table 3. Other ions were neglected since their optical depths are negligibly small. To run the simulation, we adopted an input spectral model of optically thin plasma generated with *bapec*. The emission model includes all emission lines, including the weak satellite lines.

We examined three assumptions for the velocity ($\sigma_{\rm v}$) field based on the line-of-sight velocity dispersion shown in the "V" paper: a uniform $\sigma_{\rm v}$ of 150 km s^{-1} (case 1) as

Table 4. Assumed velocity field of the one-component velocity (σ_v) in our simulation with `Geant4`.

Case ID	$\sigma_{v,1D}$ (km s^{-1})					
	$r < 0\rlap{.}'5$	$0\rlap{.}'5 < r < 1'$	$1' < r < 2'$	$2' < r < 5'$	$r > 5'$	Temp. model*
Case 1	150	150	150	150	150	Nominal
Case 1a	150	150	150	150	150	Nominal+ 10%
Case 2	200	200	150	150	100	Nominal
Case 3	200	200	150	100	100	Nominal
Case 4	200	150	150	150	150	Nominal
Case 5	200	200	150	100	300	Nominal

*Assumed "nominal" temperature model as shown in figure 7. We estimate the temperature uncertainties changing the temperature by +10%, which corresponds to the azimuthal dependence of the temperature profile from Chandra and XMM.
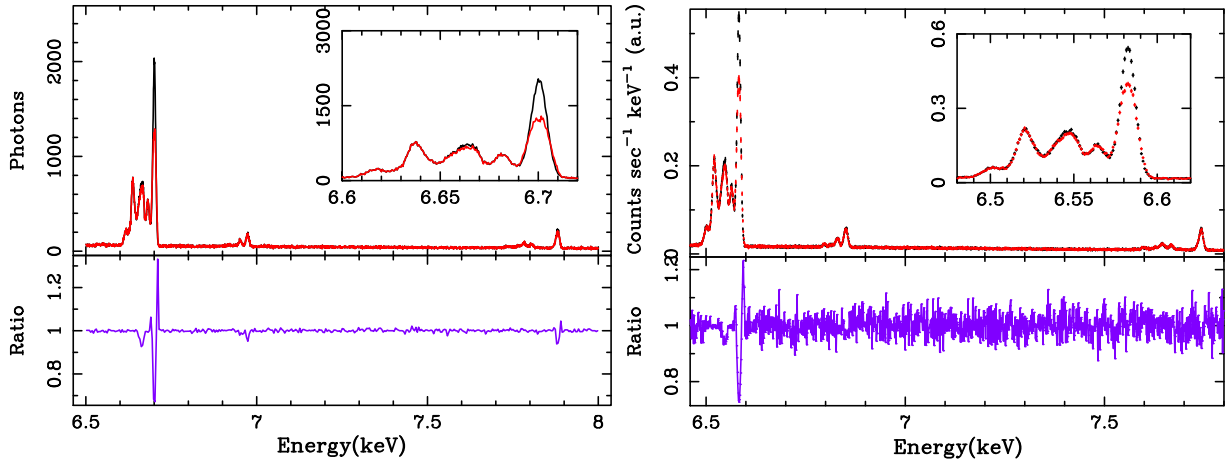
Fig. 9. Left: Photon lists generated by the `Geant4` simulator assuming a uniform σ_v profile of 150 km s^{-1} (case 1) for the inner, $0\rlap{.}'5$ (radius), region in Perseus (top panel). The red and black lines correspond to simulations with and without RS, respectively. Right: mock spectra for the obs23_cen region with the HEAsim tool with the photon lists generated by the `Geant4` simulator. Small panels show a zoom-in around the Fe xxv Heα complex. The suppression of the w line in the simulated spectra is consistent with the previous results by Zhuravleva et al. (2013). (Color online)

a reference for comparison with the simulations shown in Zhuravleva et al. (2013), a peak σ_v toward the AGN and a nearly flat field elsewhere (cases 2–4), and a case in which the σ_v rises outside of the field observed by Hitomi (case 5). The parameters for each simulation are listed in table 4. Figure 9 (left panel) shows the simulated incident spectrum from the inner $0\rlap{.}'5$ radius of the cluster for a uniform σ_v of 150 km s^{-1} (case 1 in table 4). The bottom panel of the figure shows the ratio of the photon lists for the models with and without RS. The w line flux is obviously suppressed by the RS effect. Note that the suppressed w line shape is not represented by a Gaussian model which has the same σ as the w line without RS. The suppression of the w line in our simulation agrees with previous results by Zhuravleva et al. (2013). On the other hand, the predicted line broadenings due to the distortion with the `Geant4` simulator are slightly wider than those from ICMMC. However, the difference is quite negligible after being smoothed by the Hitomi responses as described in the next paragraph.

After generating the projected photon lists with the `Geant4` simulator, we processed them with the HEAsim

software in Ftools to make mock event files for the Hitomi SXS FOV, taking into account the Hitomi responses. The HEAsim software calculates the redistribution of the input photons, including the Hitomi mirror and detector responses such as the effective area, the PSF, and the energy resolution. Here, we used the responses in the HEAsim tools and normalized the flux to the observed value, taking into account events out of the SXS FOV. We assumed a 1 Ms exposure time for each simulation. The black and red spectra in the right panel of figure 9 show the mock spectra for obs23_cen with and without RS, respectively, for the 150 km s^{-1} uniform σ_v (case 1) model. One can clearly see the flux suppression in the w line when RS is taken into account. As shown in the bottom panels in figure 9, the resonance line shapes are clearly distorted by the line broadening as well as the line suppression in the mock spectrum. Note that the mock spectra have finite numbers of photons since the mock spectra are normalized to a given, finite flux.

To estimate the potential impact of systematic uncertainties in the input model, we also performed simulations with the temperature and abundance profiles of the input model

changed by +10% (case 1a) and ±10%, respectively. Also, we explored the effects of the moving core within 1′, with 150 km s^{-1} in redshift relatively against the surrounding gas, as pointed out in the "V" paper (Hitomi Collaboration 2018a).

5.4 Monte Carlo simulations with the ICMMC code

In order to interpret the observed resonance line suppression and infer velocities of gas motions, we also applied a different approach, based on Monte Carlo simulations of radiative transfer in hot gas described in Zhuravleva et al. (2010)—see also Sazonov, Churazov, and Sunyaev (2002) and Churazov et al. (2004). Here, instead of simulating the whole spectrum and fitting it with plasma models to obtain line ratios, we performed calculations in specific lines. Such simulations directly provide fluxes in the considered lines for models with and without RS; their ratios, corrected for the PSF, are then compared with the observed values. This approach has been successfully applied to the analysis of RS and velocity measurements in massive elliptical galaxies and galaxy groups (Werner et al. 2009; de Plaa et al. 2012; Ogorzalek et al. 2017). In these previous works the detailed treatment of individual interactions in the simulations is described.

Since the Hitomi measurements of line broadening and variations of line centroids do not show strong radial velocity gradients in the Perseus Cluster, and the properties of the velocity field outside the inner ∼100 kpc are unknown, we conservatively assume that the velocity of gas motions is approximately the same within the considered regions. The simulations are done for a grid of characteristic velocity amplitudes, the results of which are then compared with the observed line ratios (see subsection 6.2).

6 Comparisons of the observed line ratios and the simulations

6.1 Geant4 simulations

We compared the spatial distribution of the observed line ratios with the simulations described in subsection 5.3. In order to compare the line ratios and widths, we fitted the simulated spectra with the same spectral model and responses for the ICM discussed in section 4, i.e. the "modified" *bvvapec* (*bvvapec* with the strongest lines deleted) plus Gaussian models. The mock spectra are well represented by this model. To understand the impact of limited photon statistics in the modeling, we divided the simulated event list into ten 100 ks parts, each of which had similar statistics in Fe XXV Heα to the observed Hitomi data.

Figure 5 shows comparisons of the observed and predicted line ratios and widths, and σ_v, for case 1 (flat σ_v field), with and without RS. The observed ratios of the Fe XXV Heα lines, w/z, are consistent with those from simulation with RS. The simulated ratios without RS, shown by light gray diamonds, are clearly far away from the observed ones in the inner regions. Figure 10 shows the comparisons for all models listed assuming a plausible velocity field based on the "V" paper (Hitomi Collaboration 2018a) in table 4. For all the regions, simulations of the w/z ratio for all the cases are broadly consistent with the observations as shown in figures 5 and 10. The observed widths of the w and z lines for the central region obs23_cen and the obs1_whole are well represented by the simulation with RS for cases 1, 4, and 5. The simulation for case 4 which is close to the line-of-sight velocity dispersion field in the "V" paper agrees well with the observed line ratios and widths. The simulated line widths with RS for case 2 look slightly broader than the observed one, while simulations with lower σ_v (<100 km s^{-1}) in $r > 2'$, such as case 3, are poorly described in the outer regions. Consequently, our simulation assuming a plausible velocity field based on the "V" paper is consistent with the observation, while the constant distribution and the relatively large σ_v of ∼300 km s^{-1} at large radius would not be rejected from our simulation. The simulations show that the predicted line ratios and widths are affected by the assumed velocity field rather than the RS effects. For the obs23_out region, which includes the north-west "ghost" bubble as shown in the "V" paper, the line widths from simulations are broader than observations due to the azimuthal dependence.

As for the $w/$Heβ, $w/$Lyα$_1$, and $w/$Lyα$_2$ lines, the simulated ratios with the RS effects also broadly agree with the observed ones within the statistical errors, except for $w/$Lyα$_1$ in the obs23_out and obs1_whole regions. The Lyα line ratios are sensitive to the azimuthal dependence and hotter component of projected temperature. On the other hand, the observed $z/$Heβ ratios, whose lines have lower optical depth than the other lines as shown in figure 8, are also consistent with the simulated ratios.

The temperatures derived from the simulated spectra are lower than the observed ones for all the regions. It should be noted that the w/z line ratio does not change much even if the temperature and σ_{v+th} change. In fact, changing the temperature in simulations by +10% for case 1a, which corresponds to the azimuthal scattering, does not change the results within the observed statistical errors. The derived σ_v for cases 1, 4, and 5 agree well with the observations in the innermost region, while those in the obs23_out region are lower than the simulated ones. We also estimated the uncertainties by changing the Fe abundance by ±10%. The resultant line ratios do not change by more than ∼3%.
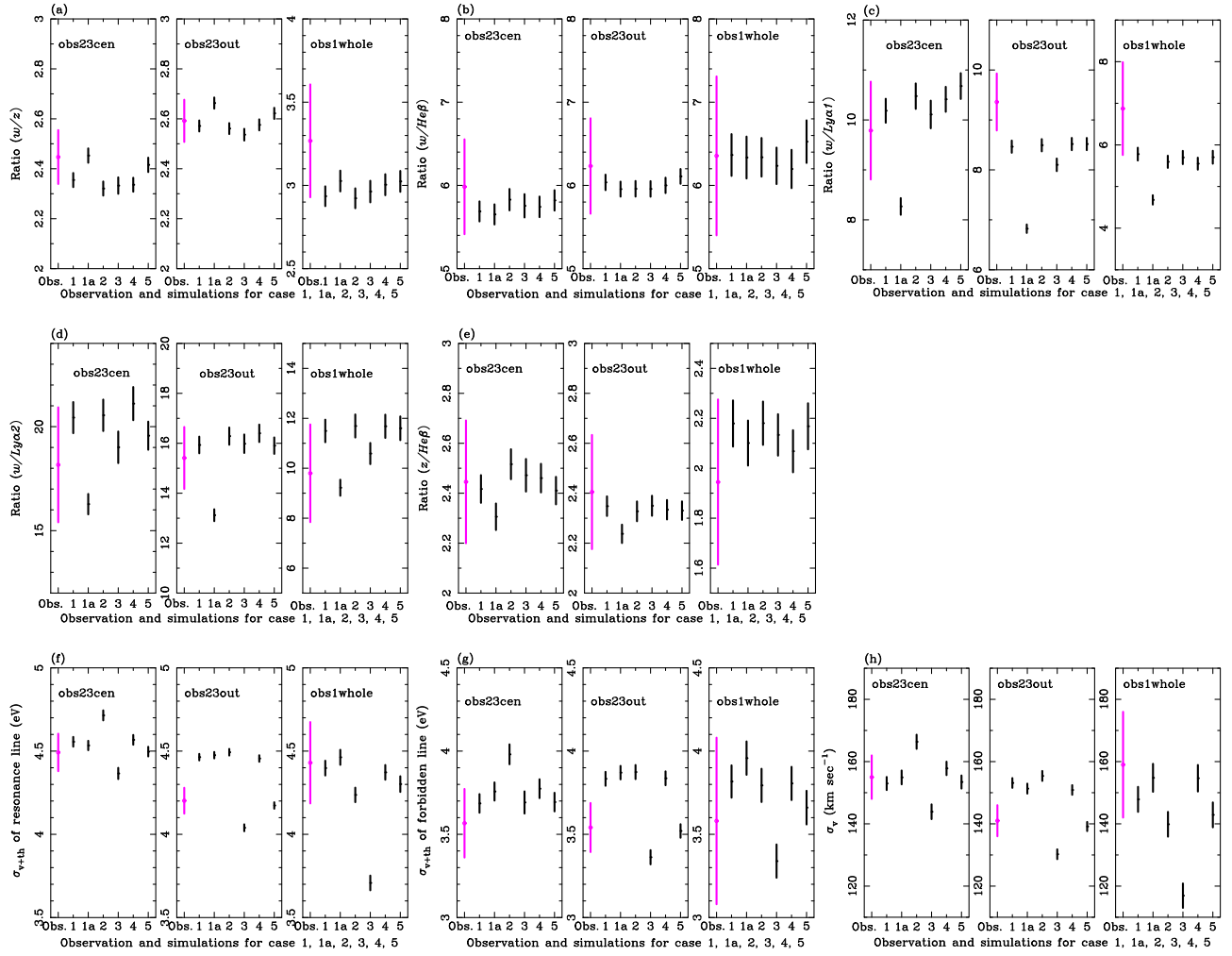
Fig. 10. (a)–(e): Comparisons of line ratios of the Fe Heα resonance (w) to forbidden (z), Heβ, and Ly$\alpha_{1,2}$, and the Fe Heα w to Heβ between observation (magenta, noted as Obs.) and simulations with RS for case 1, 1a, 2, 3, 4, and 5. (f)–(g): Same as line widths of the w and z. (h): Same as the derived σ_v from the mock spectra. (Color online)

In this simulation, we assumed spherical symmetry in the cluster core. If bulk motion existed along the line of sight in the cluster core, the line widths should be broader along the line of sight. The "V" paper (Hitomi Collaboration 2018a) actually shows a large-scale bulk velocity gradient of $\sim$100 km s^{-1}. As shown in section 4, we adopted the gain correction, which gave $\sim$5% broader line widths than the uncorrected data, but the "V" paper did not. In order to estimate the uncertainties, we performed simulations with the assumption of the core moving within the $0\rlap{.}'5$ radius with 150 km s^{-1} relative to the surrounding gas based on case 1. The resultant w/z line ratios in obs23_cen did not change within the statistical errors for case 1. Therefore, we confirmed that the RS effect is not very sensitive to bulk motion in the Perseus Cluster core, as was also shown previously by Zhuravleva et al. (2011). On the other hand, the derived w and z line widths are broader by 2% and 1% than those from case 1, and also 4% and 3% wider

than the observation. These discrepancies are smaller than the difference between the gain-corrected and uncorrected data as shown in figure 6.

6.2 ICMMC simulations

Using the thermodynamic model of the Perseus Cluster shown in figure 7 and the APEC (based on AtomDB version 3.0.8) plasma model, we calculated the line ratios (w/z, $w/(\mathrm{He}\beta_1 + \mathrm{He}\beta_2)$, $w/\mathrm{Ly}\alpha_1$, and $w/\mathrm{Ly}\alpha_2$) as a function of projected distance from the cluster center, assuming different levels of isotropic turbulence and accounting for RS. The results of simulations were then combined with the 2D PSF maps of Hitomi provided by the "V" paper (Hitomi Collaboration 2018a). The results for the w/z ratio are shown in the top left panel in figure 11. The uncertainties on the line ratios are a result of a series of simulations in which we varied the assumed temperature, density, and
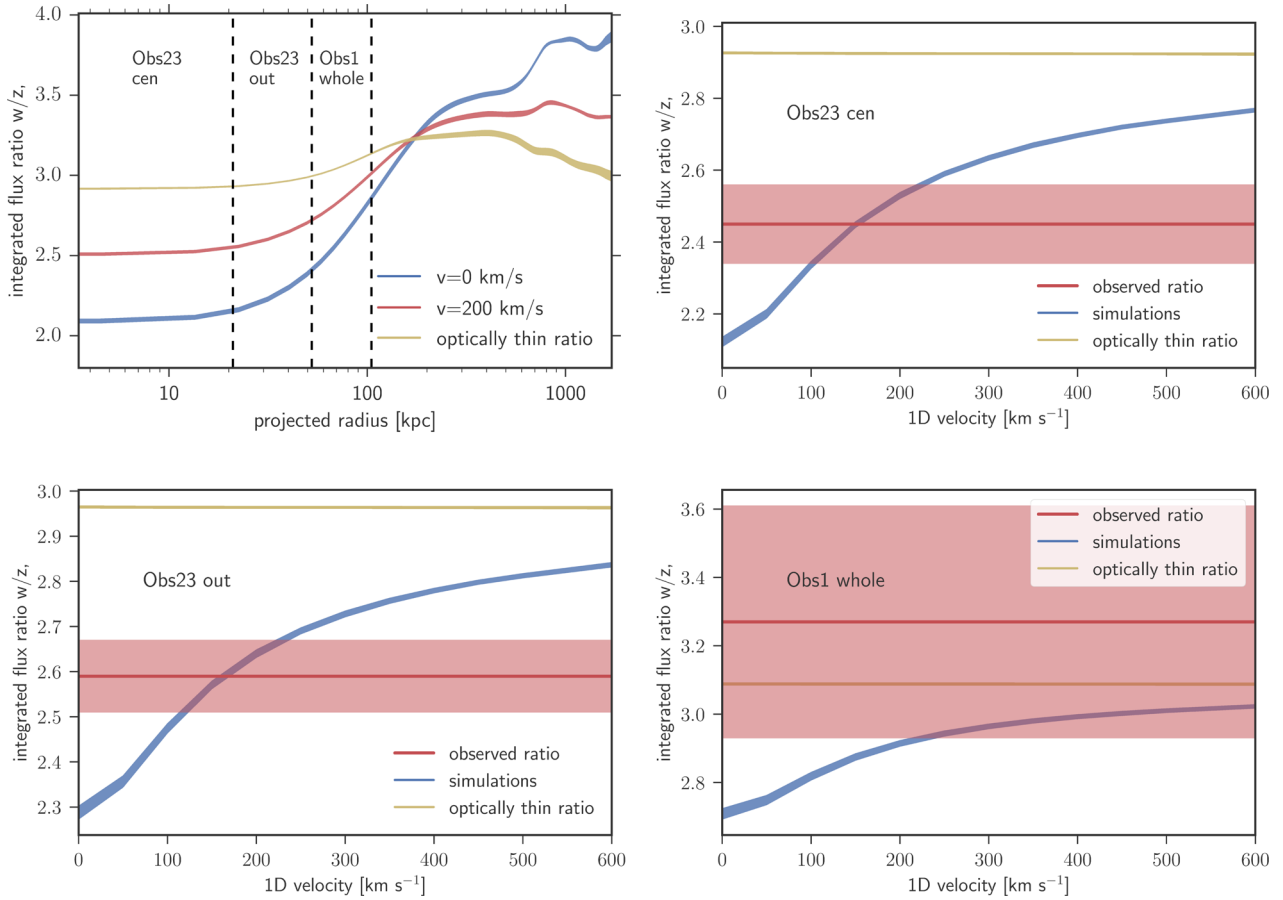
Fig. 11. Top left: w/z ratio as a function of projected distance from the cluster center calculated using ICMMC simulations of RS assuming zero (blue) and 200 km s^{-1} (red) velocity of gas motions along the line of sight. The optically thin line ratio is shown in yellow. All ratios are combined with the Hitomi PSF. The width of each curve reflects the 1 σ statistical uncertainty on the deprojected thermodynamic profiles (see figure 7). The approximate locations of the spectral extraction regions (obs23_cen, obs23_out, and obs1_whole) are shown with dashed lines. Top right and bottom: integrated flux ratio over spectral extraction regions (see figure 1) as a function of line-of-sight velocity (blue); integrated optically thin line ratio vs. velocity (yellow) and the observed line ratio from the Hitomi data (red). The overlap between the red regions and blue curves provides constraints on the velocity of gas motions. (Color online)

abundance profiles within the uncertainties for the cluster model shown in figure 7. These flux ratios are integrated over the observed regions (obs23_cen, obs23_out, and obs1_whole, see figure 1) and compared with the observed line ratios. The rest of the panels in figure 11 show the w/z ratio spatially integrated within the observed regions as a function of the one-component (1D) velocity. As expected, the larger the velocity, the closer the line ratio to the optically thin case. The observed line ratios are plotted in red. The overlap between the observed and theoretical line ratios allows us to constrain the velocity of gas motions. Note that the RS effect is the smallest in the obs1_whole region. Also, the statistical uncertainty on the measured w/z ratio is the largest in this region. Therefore, a longer Hitomi-like observation will be required for a positive velocity measurement using the RS effect for the region obs1_whole.

For each line ratio, the results of the simulations (blue regions in figure 11) are then combined with the measured error distributions in the observed line ratios (red regions), and probability distributions for turbulent velocities are obtained, as shown in figure 12 (see Ogorzalek et al. 2017 for the method). Assuming that the maximum Mach number, $M_{max} = \sqrt{3} V_{los}/c_s$, of gas motions is unity, 1 σ confidence intervals on the velocity measurements are obtained (blue regions in figure 12). The velocity distributions obtained from the w/z line ratio are peaked, and the confidence intervals are relatively insensitive to the choice of M_{max} in both obs23_cen and obs23_out regions. The measured turbulent velocities are 150^{+80}_{-56} km s^{-1} and 162^{+78}_{-50} km s^{-1} in these regions, consistent with the direct velocity measurements through line broadening (Hitomi Collaboration 2016). In contrast, the velocity distributions inferred from the $w/(He\beta_1 + He\beta_2)$ (hereafter, $w/He\beta$)
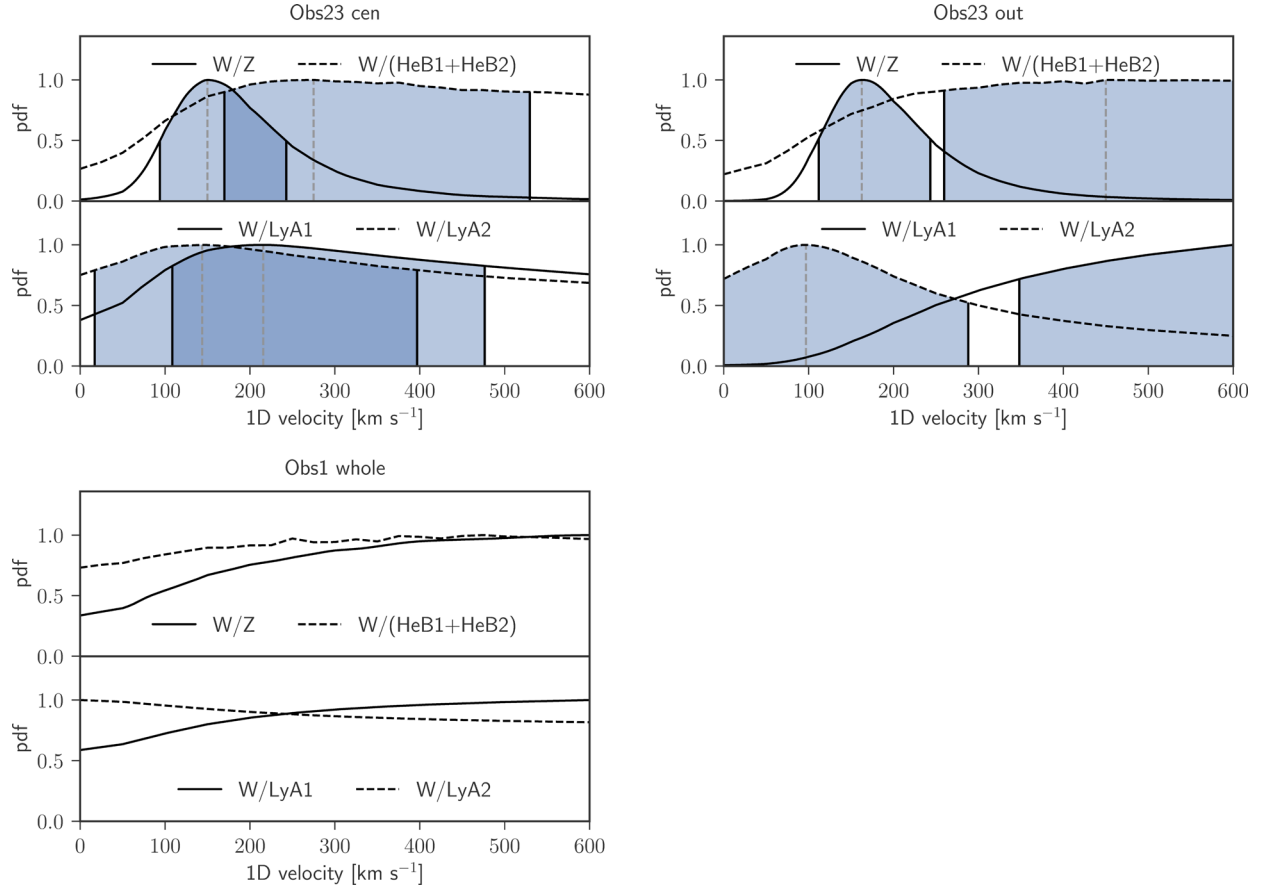
Fig. 12. Velocity probability distributions from the convolution of the observed line ratios and those predicted from numerical simulations of radiative transfer in Perseus combined with the Hitomi PSF. The three considered regions are shown in the top left, top right, and bottom panels. Confidence intervals, measured under the assumption that the maximum Mach number is unity, are shown in blue. See the legend for different line ratios. (Color online)

line ratio is quite uncertain and depends on the assumed maximal Mach number. Longer, Hitomi-like, observations will improve the results for this ratio. The ratios $w/\mathrm{Ly}\alpha_1$ and $w/\mathrm{Ly}\alpha_2$ in the obs23_cen region provide velocities $220^{+260}_{-111}\,\mathrm{km\,s^{-1}}$ and $144^{+256}_{-127}\,\mathrm{km\,s^{-1}}$, respectively. In the outer region, $w/\mathrm{Ly}\alpha_2$ gives a velocity of $97^{+193}_{-97}\,\mathrm{km\,s^{-1}}$, consistent with the direct velocity measurements, while the $w/\mathrm{Ly}\alpha_1$ ratio gives a 2σ lower limit of $178\,\mathrm{km\,s^{-1}}$. The latter result is very sensitive to the choice of M_{max}. Note that the $\mathrm{Ly}\alpha$ lines of He-like Fe have the peaks of their emissivity times ionic fraction at gas temperatures $\sim 10\,\mathrm{keV}$, while the same quantity for the w line of He-like Fe peaks around $\sim 5\,\mathrm{keV}$. Since our thermodynamic model for Perseus is calculated from 0.5–8.5 keV band spectra, the contribution of high-temperature gas could be underrepresented in our fiducial cluster model, which would affect the emissivity of the $\mathrm{Ly}\alpha$ lines. Therefore, the $w/\mathrm{Ly}\alpha$ line ratios are the least reliable of the ratios considered here. The bottom panel in figure 12 shows the velocity distributions measured in the obs1_whole region, for which the constraints are weak (see also figure 11).

Our interpretation of the observed line suppressions due to RS relies on the assumption of spherical symmetry and the choice of the reference emissivity model for an optically thin plasma. Below, we check how these assumptions affect the result as well as the effect of the Hitomi PSF.

6.2.1 Hitomi PSF
For correct interpretation of the observed line ratios, it is important to take the Hitomi PSF into account. The sensitivity of the results to the PSF is shown in the top panels in figures 13 and 14, where the PSF-corrected (default) and PSF-uncorrected results are shown in gray and red, respectively. The peaks of the distributions for the w/z ratio change by a factor of ~ 2 and by $\sim 20\%$ in the central and outer regions, correspondingly. Results for the $w/\mathrm{He}\beta$ ratio are almost unaffected by the PSF in contrast to the $w/\mathrm{Ly}\alpha$ ratios. The PSF correction always brings the peak velocity closer to the directly measured value (Hitomi Collaboration 2018a).
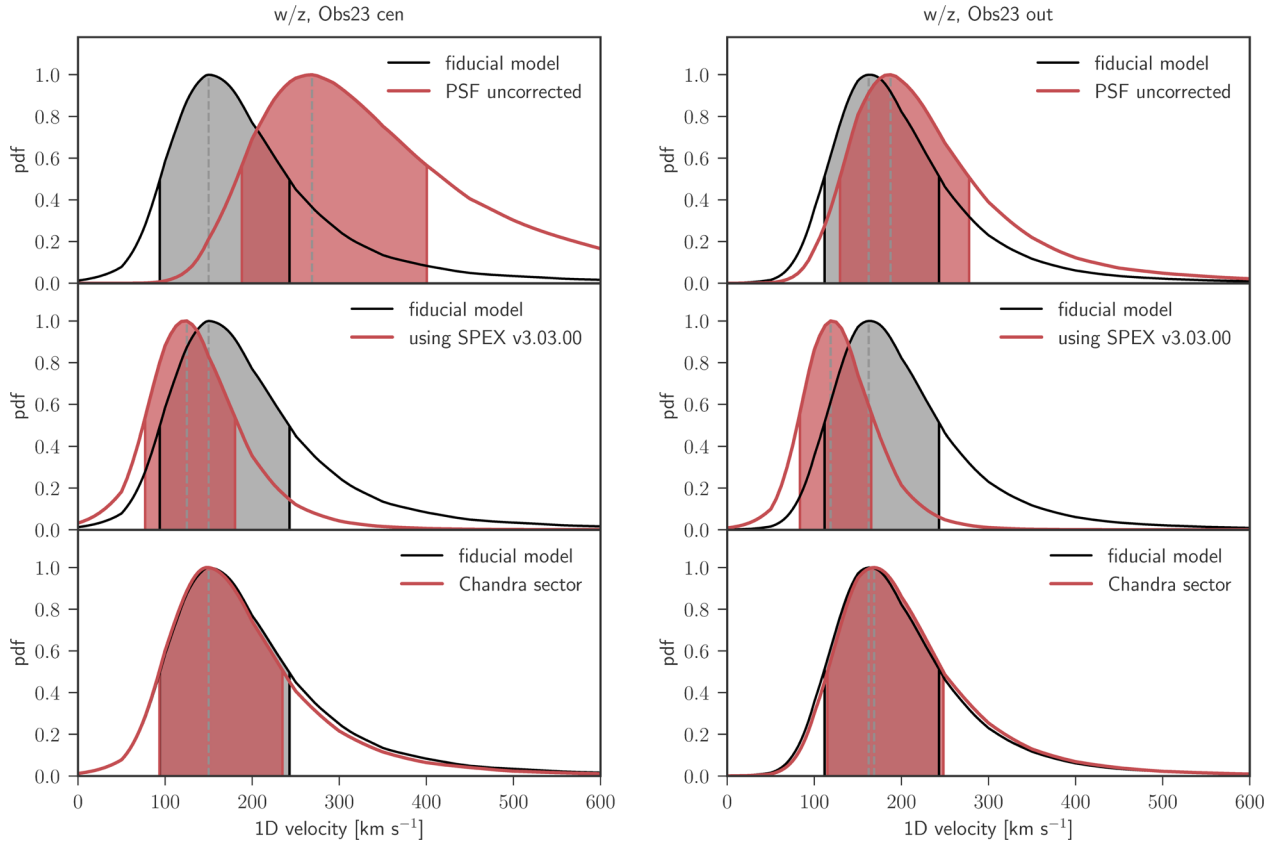
Fig. 13. Sensitivity of the measured velocity of gas motions in Perseus from the w/z line ratio to (from the top) the Hitomi PSF, the choice of optically thin plasma model, and assumption of spherical symmetry for the regions obs23_cen on the left and obs23_out on the right. (Color online)

6.2.2 Model for the optically thin plasma

Our simulations are based on the APEC model for an optically thin plasma. However, the line emissivities are slightly different in the SPEX plasma model (Kaastra et al. 1996), as discussed in the "A" paper (Hitomi Collaboration 2018c). Though such differences have little affect on the overall parameters of the best-fitting spectral models, they might be significant for more subtle plasma diagnostics such as the RS. We have therefore implemented the SPEX v3.03.00 model in our simulations and redone the analysis. Following the "A" paper, the ionization balance is set to Urdampilleta, Kaastra, and Mehdipour (2017) instead of the default one by Bryans, Landi, and Savin (2009). The calculations by Urdampilleta, Kaastra, and Mehdipour (2017) provide inner-subshell ionization contributions to the spectrum, which are compatible with the SPEX code.

The results based on both plasma models are consistent within the uncertainties, as shown in figures 13 and 14 (middle panels). The measured w/z line ratio velocity shifts from 150^{+80}_{-50} km s^{-1} (162^{+78}_{-50} km s^{-1}) with APEC to 125^{+55}_{-48} km s^{-1} (119^{+46}_{-36} km s^{-1}) with SPEX in obs23_cen (obs23_out); see figure 13.

6.2.3 Spherical symmetry

Our Perseus model is calculated assuming spherical symmetry, which will not be correct in detail given the complex structure of the cluster core. To test this assumption, we re-measured the thermodynamic properties of the cluster from the Chandra data, limiting the analysis to a sector that contains Hitomi pointings, and repeated the analysis described above for this model. The results for the w/z ratio are essentially unaffected, as shown in the bottom panels of figure 13. The peak of the velocity distribution inferred from the $w/Ly\alpha2$ line ratio decreases by a factor of $\sim$2 in the outer region, although the results remain consistent within uncertainties (figure 14, bottom right panel). In all other cases the peak velocity changes by an even smaller factor, typically by less than 10%.

Improvements in the results from the w/z line ratio will require refinements of the details of the plasma models for these lines. The SPEX plasma model predicts a stronger RS effect in the cluster core than APEC. The $w/He\beta$ results, in contrast, are limited by statistical uncertainties and can easily be improved with longer, Hitomi-like, observations. Further improvements for the $w/Ly\alpha1$ and $w/Ly\alpha2$ line
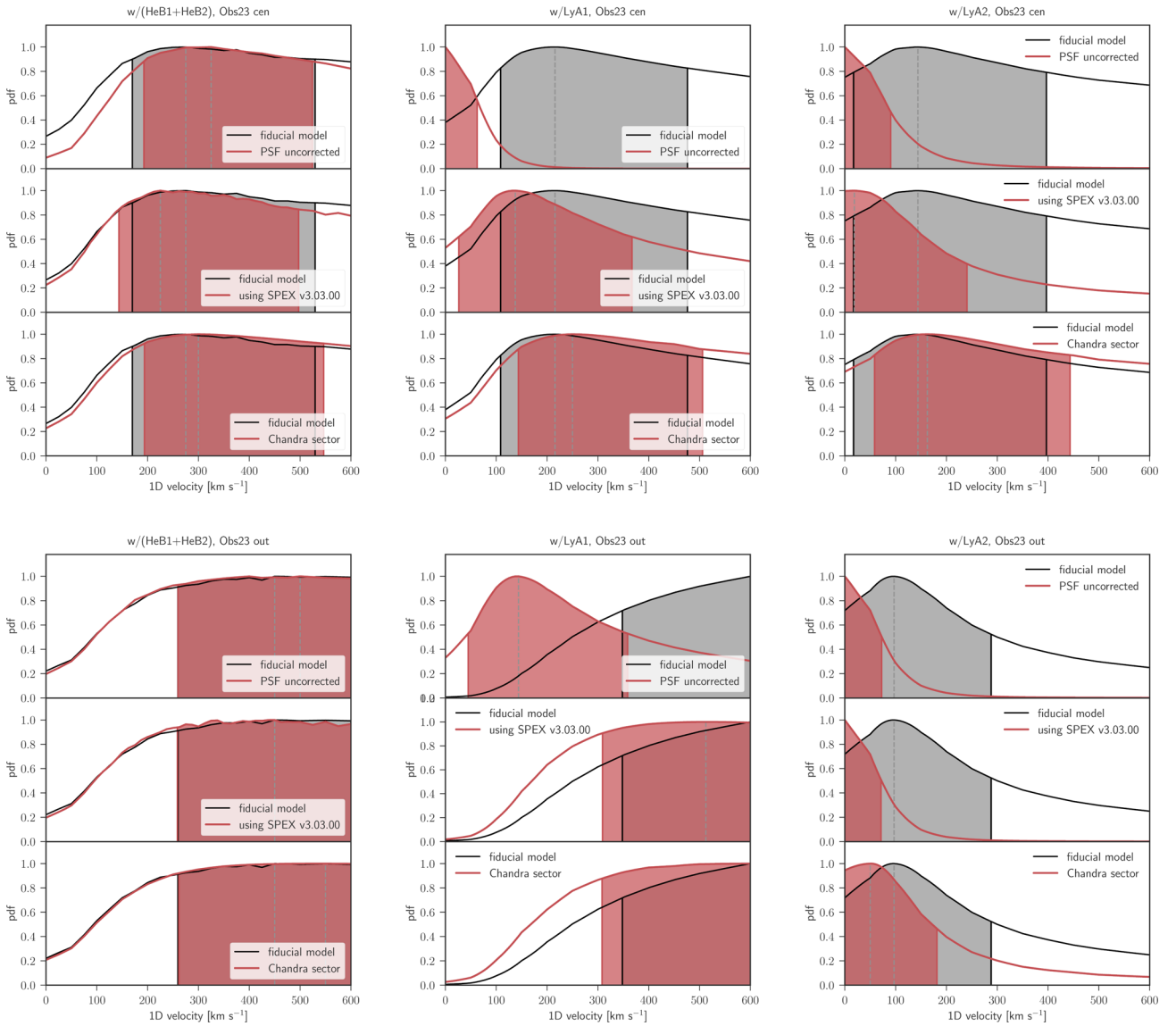
Fig. 14. Same as figure 13, for the rest of the considered line ratios. Results in obs23_cen (obs23_out) are shown in the top (bottom) panels. (Color online)

ratios will require a more detailed model of the Perseus Cluster, in particular the contribution of the gas component with $T > 5\,\mathrm{keV}$.

7 Uncertainties in the atomic excitation rates

In this section, systematic uncertainties in the observed line ratios arising from uncertainties in calculated atomic parameters are discussed. The focus will be on parameters that most directly affect the manifestation of RS, i.e., the optical depth of the resonance line, w, and the intensity ratio w/z.

The optical depth at line center is proportional to a line's absorption oscillator strength (Zhuravleva et al. 2013),

which depends on the upper level's radiative rate, and in turn is directly related to the natural line width. Hence, as an estimate of the uncertainty of the oscillator strength, we compare the natural line width, $\Delta E^{\mathrm{Nat.}}$, of line w in APEC (AtomDB 3.0.8) and SPEX 3.03 (which are based on different atomic structure calculations) to the measured line width from laboratory measurements by Rudolph et al. (2013). The agreement between the measured values and those found in SPEX and APEC is good: $\Delta E^{\mathrm{SPEX}} = 0.301\,\mathrm{eV}$, $\Delta E^{\mathrm{APEC}} = 0.308\,\mathrm{eV}$, $\Delta E^{\mathrm{Meas.}} = 0.311 \pm 0.01\,\mathrm{eV}$ (Rudolph et al. 2013). Based on this comparison, the systematic error in the oscillator strength is estimated to be $<5\%$.

The error associated with the optically thin intensity ratio w/z is more complex. It includes errors in the

total collisional excitation cross-sections, errors associated with unresolved satellites, and contributions from charge exchange recombination. The dominant excitation mechanism for populating the upper state of line w in a thermal plasma is electron impact excitation (EIE) from the ground state. The total effective EIE cross-sections have been measured (Wong et al. 1995; Hell 2017) at a few single electron impact energies using an electron beam ion trap. These measurements do not include contributions from dielectronic satellites. While it is not possible to compare the results of the measurements directly to the output of SPEX and APEC (because neither model provides cross-sections as a function of electron impact energy, but rather produces electron-temperature-dependent, unitless collision strengths) it is possible to compare the measurement results to the EIE cross-sections calculated using the same theoretical method used to produce the collision strengths in APEC and SPEX, i.e., the methods of Aggarwal and Keenan (2013) and of Zhang and Sampson (1990), respectively. This comparison shows good agreement, i.e., well within the ∼10% error of the measurement (Hell 2017). Given this agreement, and the agreement among calculations, the error on the total electron impact excitation rate of line w is estimated to be <10%.

The forbidden line z has a significantly more complicated excitation structure. As detailed in the "Atomic" paper (Hitomi Collaboration 2018c), the upper level of line z is populated by a variety of mechanisms, including direct excitation from the ground state, excitation from cascades, and from innershell ionization of Li-like Fe XXIV. As a result, the uncertainty in the emissivity of line z is coupled to detailed population kinetics, in addition to the plasma model. The excitation cross-section has been measured (Wong et al. 1995) using an electron beam ion trap, and the agreement with theory is good. However, this is insufficient to estimate the total error in the line strength for a 4 keV thermal plasma.

To estimate the errors associated with w/z for a 4 keV thermal, optically thin plasma directly, the values predicted by AtomDB and SPEX are compared to results of laboratory measurement from plasmas with Maxwellian electron temperatures at coronal densities. Here, the calculations are compared to measurement using the Maxwellian simulator mode (Savin et al. 2000, 2008) employed at the LLNL EBIT-I electron beam ion trap facility. Using this mode, the spectrum of the Heα complex of Fe XXV including satellites has been measured (Gu et al. 2012). Caveats on the measurement include the fact that the average charge balance produced using the Maxwellian simulator is underionized (and thus the charge balance is not representative of a true Maxwellian) and the fact that line emission produced in an EBIT is, in general, polarized; hence, when comparing

to line ratios measured form celestial sources, polarization effects must be taken into account. The amount of polarization depends on the electron impact energy. Hence, the line emission measured using EBIT-I's Maxwellian mode, where the electron beam energy is swept across a large range, may have a range of polarization values. The calculated polarization of line w ranges from 0.6 to 0.4 between the threshold for excitation and an electron impact energy of 24 keV. The polarization of line z is ∼−0.08 near threshold and −0.22 above threshold for population by cascades (Hakel et al. 2007). The agreement with theory is good, although the uncertainty in the measurements remains relatively large, i.e., on the order of 20%–30% (Beiersdorfer et al. 1996; Hakel et al. 2007).

Here, polarization effects are taken into account by setting the polarization of line w to $P = 0.5$ and of line z to $P = -0.22$. No energy dependence is included because the correction factor to the w/z line ratio across the entire range of polarization only varies by ∼5%, and because the true polarization of lines z and w is not known due to depolarization effects (Gu et al. 1999). The difference between the polarization-corrected ratio and the uncorrected ratio is 11%, i.e., the polarization-corrected w/z ratio is 2.92 ± 0.2 and the uncorrected ratio is 3.25 ± 0.07. The errors in these ratios include the uncertainty in the polarization, the spectrometer response, and statistics.

The measured ratio is also systematically lower than the ratio for a true Maxwellian because the large amount of Li-like Fe XXIV present in the EBIT results in a larger contribution to z from innershell ionization. The measured ratio has to be corrected based on a comparison of the ionization balance in the EBIT in its Maxwellian simulator mode with the true thermal ionization balance in a 4 keV plasma, and the fraction of the emissivity in z due to innershell ionization. However, according to calculations, for a 4 keV plasma, the contribution from innershell ionization is only a ∼10% enhancement of line z in the EBIT case. While the measured value at EBIT is therefore $w/z = 2.92 \pm 0.2$, the corrected ratio may be as high as $≈1.1 \times 2.92 = 3.21 \pm 0.2$. This value is fully consistent with the ratio at $kT = 4$ keV in APEC of $w/z = 2.98$ and SPEX v3.03 of $w/z = 3.11$ (see figure 15). It should be noted that the Fe XXV Heα complex, as well as other He-like systems, have been measured in tokamak plasmas where no polarization effects are present (Bitter et al. 2008); however, those measurements are at lower temperatures. Comparison of the lower-temperature data with the predictions from SPEX and APEC would be useful.

In a 4 keV plasma, unresolved dielectronic recombination (DR) satellites contribute to the fluxes of line w and line z, and uncertainties in their contributions to w and z should be estimated. In the case of line w, the
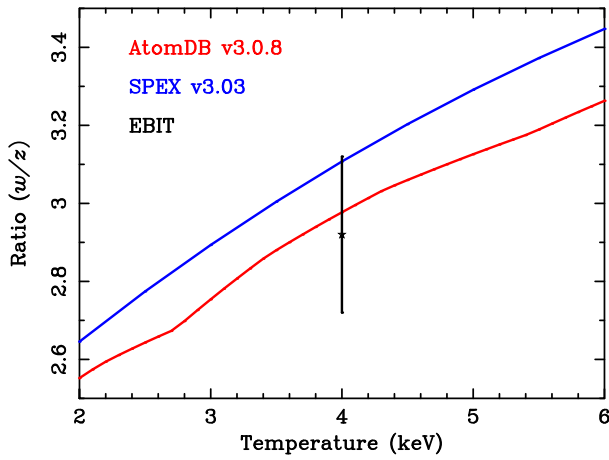
Fig. 15. Temperature dependence of the *w/z* ratio for AtomDB version 3.0.8, SPEC v3.03, and EBIT measurement. (Color online)

emission from high-*n* DR ($n \geq 3$) satellites blends with line *w*. These satellite intensities have been measured in detail by Beiersdorfer et al. ([1992a]) and also by Watanabe et al. ([2001]). The agreement between theory and experiment is good (Watanabe et al. [2001]). We can get a rough estimate of the uncertainty in the intensity of *w* due to uncertainties in the intensities of the unresolved satellites as follows. In the "Atomic" paper, calculated satellite intensities are listed in table 11, where calculations from three separate plasma models are compared, assuming collisional equilibrium at $kT = 4$ keV. Four $n = 3$ satellites have a summed intensity of 0.065 of the intensity of *w*. The dispersion between the models has a standard deviation of about 10% of this relative intensity. Likewise, three $n = 4$ satellites have a summed intensity relative to *w* of 0.018, with a standard deviation of about 10% of this value. The dispersion between the models compares well to the intensity measurement error of about 10% quoted by Watanabe et al. ([2001]). From these data we estimate that the uncertainty in the intensity of *w* due to uncertainties in the unresolved satellites is of the order of 1%–2% (allowing for the presence of weaker $n > 4$ satellites).

In the case of line *z*, the most significant contribution is from the DR channel of the $1s2p^2\,{}^2D_{5/2} \rightarrow 1s^22p\,{}^2P_{3/2}$ transition, known as line *j* (Gabriel [1972]), which, although it is ~8 eV away from line *z*, is still only marginally separated in the Perseus spectrum. In addition, there is also emission from the $1s2p^2\,{}^2D_{3/2} \rightarrow 1s^22p\,{}^2P_{3/2}$ transition, known as line *l* (Gabriel [1972]), which is only about 1.5 eV above *z*, but its strength is only about 1/10 of the strength of line *j*. The strengths of both line *j* and line *l* have been measured (Beiersdorfer et al. [1992b]), with an estimated accuracy of $\lesssim 20\%$. The agreement with theoretical calculations is better than 15%. In collisional equilibrium at $kT = 4$ keV, the intensities of *j* and *l* relative to *z* are approximately 0.33

and 0.025, respectively. The uncertainty in the intensities of *j* and *l*, if completely unresolved from *z*, therefore translates into an uncertainty of about 6.5% in the estimated intensity of *z*; in practice, the dominant contributor, *j*, is partially resolved from *z* in our data, so the uncertainty due to the contribution of the satellites is significantly smaller than 6.5%. If we assign an uncertainty of 3% to *z* due to the uncertainty in the satellite contribution, and 2% to *w*, the ratio *w/z* has an uncertainty of about 4% due to possible errors in the satellite contribution.

Finally, our model for the emissivity of Fe XXV does not contain excitation by charge exchange of neutral H with Fe XXVI. The core region of the cluster does contain neutral H in close contact with the hot ICM, as is evident from the filamentary Hα emission from the core (Salome et al. [2011]). Charge exchange contributes to the intensity of both the *w* and the *z* lines, but it contributes more strongly to *z* than to *w*, and the effect therefore would tend to reduce the ratio *w/z* from its pure CIE value. In the "Atomic" paper, an explicit model for the charge exchange emission is fitted along with a CIE model. Based on the best-fit parameters for the charge exchange (which are constrained mainly by the charge-exchange predicted intensities of higher-order series members), we estimate that the process could contribute 8% of the observed flux in *z*, and 2% of the observed flux in *w*. That would lower the ratio *w/z* by 6% from its value in CIE in the central region of the cluster, which is significantly less than the suppression we observe. Moreover, charge exchange is not likely to contribute much to the emission we observe in the 1′–2′ range, where *w/z* is also significantly suppressed with respect to its value in CIE.

To summarize, when we compare the measured *w/z* ratios to the ratios predicted by the best-fitting CIE model without radiative transfer, we see a significant suppression in the innermost regions of the cluster. In the innermost region, the measured ratio is $w/z = 2.43$, while the predicted ratio is 2.98 (AtomDB 3.0.8) or 3.11 (SPEX 3.03), and the ratio measured at EBIT, corrected for systematic errors, is at least 2.92 ± 0.2. Errors in the model fluxes of unresolved satellite lines to *w* and *z* cannot account for more than a few percent of this suppression. Charge exchange excitation could account for a suppression of 6%, but only in the innermost ($r < 1'$) bin. As is expected if the suppression is due to resonance scattering of *w* photons, *w/z* tends to the "optically thin" CIE value in the outer regions of the field, and this would not be the case if the optically thin, CIE only, value we use were simply incorrect.

Comparing the results of the measured *w/z* ratio from obs23 given in table [2] with the values predicted for an optically thin plasma, and taking into account known uncertainties in the predicted values, there is very good evidence for RS in line *w*.

8 Conclusions

We have shown evidence for resonance scattering in the core of the Perseus Cluster observed with Hitomi. Namely, we observe the following: (i) the characteristic suppression of the flux of the resonance line in the Fe XXV Heα complex seen toward the center of the cluster; (ii) the expected decrease of this suppression with distance from the cluster center; and (iii) an additional broadening of the resonance line compared to other lines from the same ion. Fitting the spectra with a combination of an emission model for optically thin plasma supplemented with individual Gaussian emission lines, we measure the ratios of the resonance line flux to the fluxes in the forbidden line in the Fe XXV Heα complex, two Fe XXV Heβ lines, and the Fe XXVI Lyα lines. To interpret the observed results, we perform radiative transfer Monte Carlo simulations, assuming a spherically symmetric model for the cluster and plausible velocity fields based on direct velocity measurements (Hitomi Collaboration 2018a) including an isotropic field. Comparing the observed line ratios and the simulated values, we infer velocities of gas motions that are consistent with direct velocity measurements from line broadening. We investigate systematic uncertainties in the analysis, including the assumption of spherical symmetry, the modeling of the ICM properties, the uncertainties in line emissivities, and the contribution of charge exchange excitation.

Future, non-dispersive, high-resolution spectroscopy such as the Hitomi SXS observations will allow us to explore the effect of RS in even more detail, which, in combination with the direct velocity measurements, will provide us with a unique tool to probe the anisotropy and spatial scales of gas motions. It is important to take the RS effect into account when measuring plasma properties from high-resolution X-ray spectra of galaxy clusters. The effect can be even stronger in lower-energy lines in cooler, gas-rich systems, such as galaxy groups and large elliptical galaxies.

Hitomi's lifetime was unfortunately short. However, the micro-calorimeter at the heart of the SXS has already provided new insights with its high energy resolution. Future X-ray missions with micro-calorimeters, XARM and Athena, will be indispensable in the investigation of cluster physics.

Author contributions

K. Sato is the sub-leader of the Perseus RS team, led the data analysis and numerical simulations, and prepared the manuscript. He also contributed to the SXS hardware development, integration tests, launch campaign, in-orbit operation, and calibration. I. Zhuravleva is the sub-leader of the RS team, led the data analysis and numerical simulations, and prepared the manuscript. F. Paerels is the leader of the RS team, led the study of uncertainties in the atomic excitation rate, and prepared the manuscript. M. Furukawa, M. Ohno, K. Matsushita, and Y. Fukazawa performed numerical simulations with `Geant4` and participated in discussions. M. Ohno, Y. Fukazawa, and A. Furuzawa contributed the Hitomi hardware and in-orbit operation. A. Ogorzalek performed numerical simulations with the ICMMC code and studied the uncertainties of the plasma codes. G. Brown, A. Foster, L. Gu, and M. Leutenegger studied the uncertainties of the atomic excitation rates and codes. M. Eckart, C. Kilbourne, and M. Leutenegger contributed to the SXS hardware design, development, integration tests, launch campaign, and calibration. S. Nakashima, T. Sasaki and H. Yamaguchi helped with the modeling of the ICM structure in data analysis. S. Allen, C. Kilbourne, C. Pinto, M. Tsujimoto, M. Ozaki, and A. Simionescu helped to improve the manuscript.

Acknowledgments

Appendix. Differences between AtomDB version 3.0.8 and 3.0.9

As described in section 4, we found the residuals around 6.55 keV in the spectral fit with AtomDB version 3.0.8. This comes from the overestimation of the Li-like Fe XXIV lines in AtomDB 3.0.8. Since the corrected version 3.0.9 will be released in a few months, we re-examined the analysis with AtomDB version 3.0.9. Table 5 and figure 16 show the resultant spectral fits and parameters with AtomDB version 3.0.9. The resultant parameters are slightly changed compared to the results in the main text within the statistical errors, but the differences are negligible for our results. Table 6 and figure 17 show the optical depth and line properties with AtomDB version 3.0.9. The changes in Li-like Fe XXIV lines are separated from the He-like Fe XXV resonance and forbidden lines; these are also negligible for our simulations and conclusions.

Table 5. Same as table 2, but with AtomDB version 3.0.9

Region ID	kT^* (keV)	Fe* (solar)	$\sigma_v{}^*$ (km s^{-1})	C-stat/d.o.f.* (1.8–20 keV)	C-stat/d.o.f.[†] (6.1–7.9 keV)		
obs23_cen	3.85 ± 0.03	0.73 ± 0.01	161 ± 7	10600/11151	1797/1784		
obs23_out	3.98 ± 0.01	0.73 ± 0.01	147 ± 5	14518/11744	1930/1784		
obs1_whole	4.99 ± 0.09	0.57 ± 0.03	163 ± 18	6324/6930	1277/1494		

Region ID Line ratio	$w/z^\dagger$	$w/\mathrm{He}\beta^\dagger$	$w/\mathrm{Ly}\alpha_1{}^\dagger$	$w/\mathrm{Ly}\alpha_2{}^\dagger$	$z/\mathrm{He}\beta^\dagger$	$z/\mathrm{Ly}\alpha_1{}^\dagger$	$z/\mathrm{Ly}\alpha_2{}^\dagger$
obs23_cen	2.34 ± 0.10	5.80 ± 0.55	9.62 ± 0.95	17.74 ± 2.04	2.48 ± 0.25	4.10 ± 0.42	7.57 ± 0.30
obs23_out	2.50 ± 0.08	6.06 ± 0.56	9.26 ± 0.57	15.16 ± 1.22	2.43 ± 0.23	3.70 ± 0.24	6.07 ± 0.21
obs1_whole	3.18 ± 0.33	6.21 ± 0.92	6.86 ± 1.12	9.74 ± 1.95	1.95 ± 0.33	2.16 ± 0.39	3.07 ± 0.36

Region ID Line width (σ_{v+th})	$w^\dagger$ (eV)	$z^\dagger$ (eV)	$\mathrm{Ly}\alpha^\dagger$ (eV)	$\mathrm{He}\beta^\dagger$ (eV)			
obs23_cen	4.40 ± 0.11	3.78 ± 0.22	5.29 ± 0.58	3.43 ± 0.51			
obs23_out	4.12 ± 0.08	3.68 ± 0.15	3.44 ± 0.26	4.26 ± 0.45			
obs1_whole	4.30 ± 0.22	3.78 ± 0.51	6.09 ± 1.02	4.90 ± 0.90			

*Fits in the broad band of 1.8–20.0 keV with the AGN and modified *bvvapec* models which exclude only the resonance line and add the line with the Gaussian model. σ_v is a turbulent velocity in the *bvvapec* model without the resonance line. The numbers in this table are slightly smaller than those in the "V" paper (Hitomi Collaboration 2018a), which are from the difference of the energy band in the spectral fits.

[†]Fits in the narrow band of 6.1–7.9 keV with the AGN and modified *bvvapec* models which exclude the He-α resonance and forbidden, He-β1&2, and Ly-α1&2 lines.
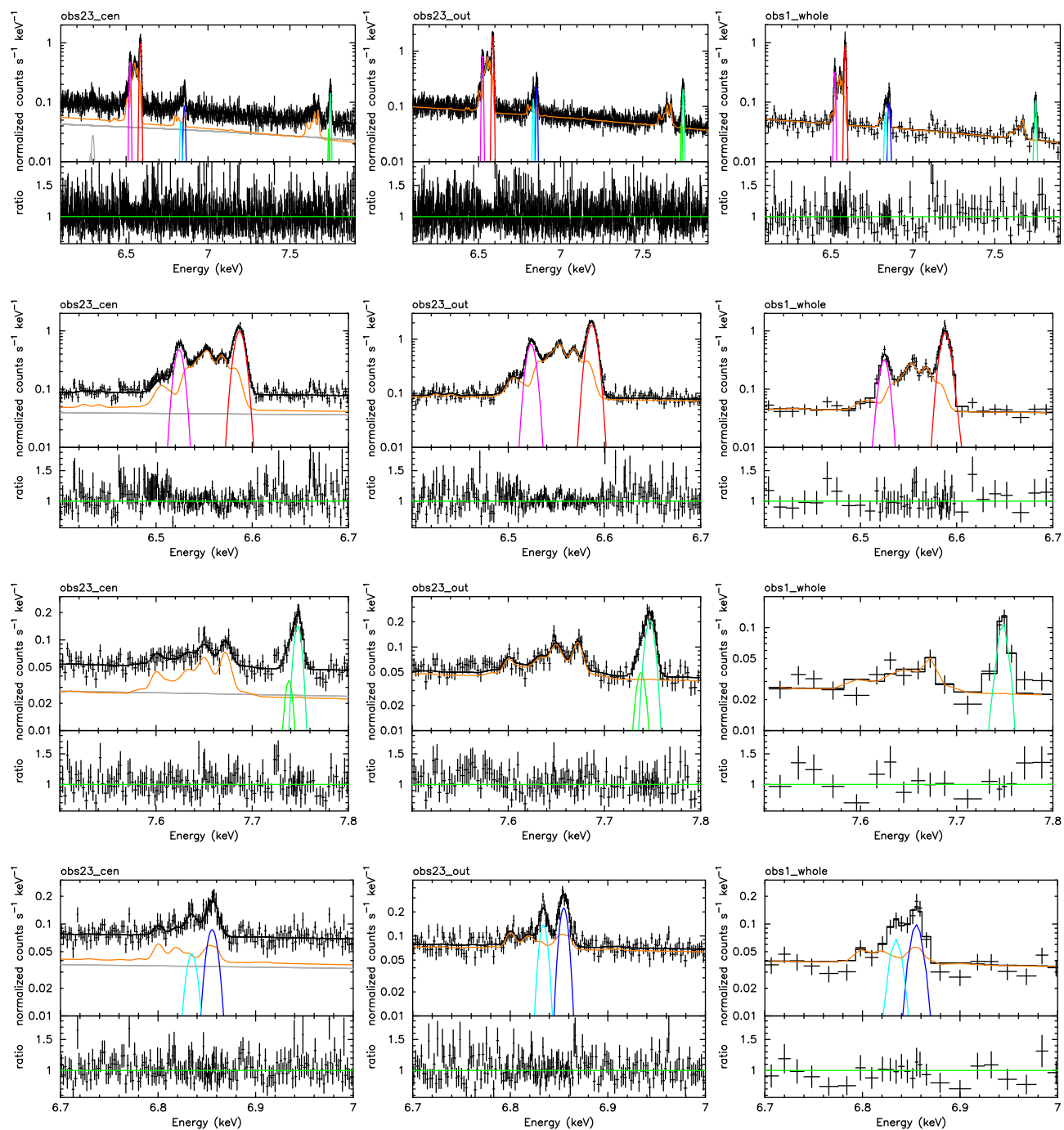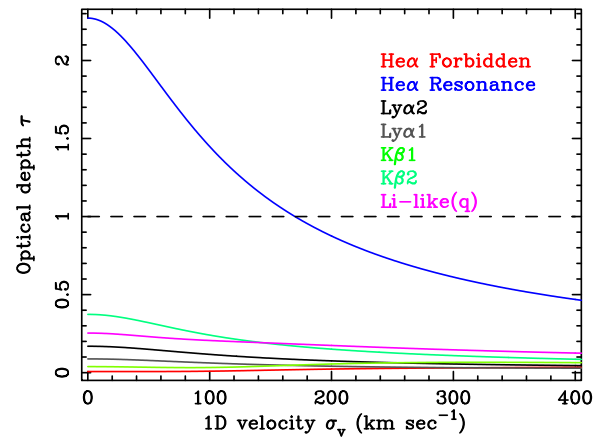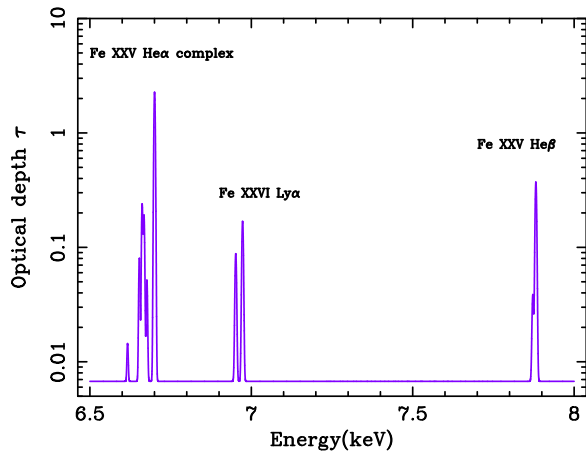
Fig. 16. Same as figure 2, but with AtomDB version 3.0.9. (Color online)

Table 6. Same as table 3, but with AtomDB 3.0.9.

Ion	Energy (eV)	Lower level*	Upper level*	Oscillator strength	Optical depth τ ($\sigma_v = 0\,\mathrm{km\,s^{-1}}$)	Comments*
Fe XXIV	6616.73	$1s^2 2s_{1/2}\,^2S_{1/2}$	$1s_{1/2}2s_{1/2}2p_{1/2}\,^4P_{3/2}$	1.63×10^{-2}	1.45×10^{-2}	u
Fe XXV	6636.58	$1s^2\,^1S_0$	$1s2s\,^3S_1$	3.03×10^{-7}	6.75×10^{-3}	Heα, z
Fe XXIV	6653.30	$1s^2 2s_{1/2}\,^2S_{1/2}$	$1s_{1/2}2s_{1/2}2p_{1/2}\,^2P_{1/2}$	1.57×10^{-1}	8.04×10^{-2}	r
Fe XXIV	6661.88	$1s^2 2s_{1/2}\,^2S_{1/2}$	$1s_{1/2}2s_{1/2}2p_{3/2}\,^2P_{3/2}$	4.89×10^{-1}	2.39×10^{-1}	q
Fe XXV	6667.55	$1s^2\,^1S_0$	$1s_{1/2}2p_{1/2}\,^3P_1$	5.79×10^{-2}	1.92×10^{-1}	Heα, y
Fe XXIV	6676.59	$1s^2 2s_{1/2}\,^2S_{1/2}$	$1s_{1/2}2s_{1/2}2p_{3/2}\,^2P_{1/2}$	9.62×10^{-2}	5.18×10^{-2}	t
Fe XXV	6682.30	$1s^2\,^1S_0$	$1s_{1/2}2p_{3/2}\,^3P_2$	1.70×10^{-5}	7.26×10^{-3}	Heα, x
Fe XXV	6700.40	$1s^2\,^1S_0$	$1s_{1/2}2p_{3/2}\,^1P_1$	7.19×10^{-1}	2.27	Heα, w
Fe XXVI	6951.86	$1s$	$2p_{1/2}$	1.36×10^{-1}	8.81×10^{-2}	Lyα_2
Fe XXVI	6973.07	$1s$	$2p_{3/2}$	2.73×10^{-1}	1.69×10^{-1}	Lyα_1
Fe XXV	7872.01	$1s^2\,^1S_0$	$1s3p\,^3P_1$	1.18×10^{-2}	3.87×10^{-2}	Heβ_2, intercomb.
Fe XXV	7881.52	$1s^2\,^1S_0$	$1s3p\,^1P_1$	1.37×10^{-1}	3.73×10^{-1}	Heβ_1, resonance

*Letter designations for the transitions as per Gabriel (1972).

Fig. 17. Same as figure 8, but with AtomDB version 3.0.9. (Color online)

References

Aggarwal, K. M., & Keenan, F. P. 2013, Phys. Scr., 87, 055302

Ahoranta, J., Finoguenov, A., Pinto, C., Sanders, J., Kaastra, J., de Plaa, J., & Fabian, A. 2016, A&A, 592, A145

Akimoto, F., Furuzawa, A., Tawara, Y., & Yamashita, K. 2000, Adv. Space Res., 25, 603

Angelini, L., et al. 2016, Proc. SPIE, 9905, 990514

Böhringer, H., et al. 2001, A&A, 365, L181

Beiersdorfer, P., et al. 1996, Phys. Rev. A, 53, 3974

Beiersdorfer, P., Phillips, T. W., Wong, K. L., Marrs, R. E., & Vogel, D. A. 1992, Phys. Rev. A, 46, 3812

Beiersdorfer, P., Schneider, M. B., Bitter, M., & von Goeler, S. 1992, Rev. Sci. Inst., 63, 5029

Bitter, M., Hill, K. W., Goeler, S. V., Stodiek, W., Beiersdorfer, P., Rice, J. E., & Ince-Cushman, A. 2008, Canadian J. Phys., 86, 291

Bryans, P., Landi, E., & Savin, D. W. 2009, ApJ, 691, 1540

Churazov, E., Forman, W., Jones, C., & Böhringer, H. 2003, ApJ, 590, 225

Churazov, E., Forman, W., Jones, C., Sunyaev, R., & Böhringer, H. 2004, MNRAS, 347, 29

Churazov, E., Zhuravleva, I., Sazonov, S., & Sunyaev, R. 2010, Space Sci. Rev., 157, 193

de Plaa, J., Zhuravleva, I., Werner, N., Kaastra, J. S., Churazov, E., Smith, R. K., Raassen, A. J. J., & Grange, Y. G. 2012, A&A, 539, A34

Ezawa, H., et al. 2001, PASJ, 53, 595

Foster, A. R., Ji, L., Smith, R. K., & Brickhouse, N. S. 2012, ApJ, 756, 128

Gabriel, A. H. 1972, MNRAS, 160, 99

Gilfanov, M. R., Syunyaev, R. A., & Churazov, E. M. 1987, Soviet Astron. Lett., 13, 3

Grant, I. P. 1974, J. Physics B, 7, 1458

Gu, M. F., Beiersdorfer, P., Brown, G. V., Graf, A., Kelley, R. L., Kilbourne, C. A., Porter, F. S., & Kahn, S. M. 2012, Can. J. Phys., 90, 351

Gu, M. F., Savin, D. W., & Beiersdorfer, P. 1999, J. Phys. B, 32, 5371

Hakel, P., Mancini, R. C., Harris, C., Neill, P., Beiersdorfer, P., Csanak, G., & Zhang, H. L. 2007, Phys. Rev. A, 76, 012716

Hayashi, K., Fukazawa, Y., Tozuka, M., Nishino, S., Matsushita, K., Takei, Y., & Arnaud, K. A. 2009, PASJ, 61, 1185

Hell, N. 2017, PhD thesis, Friedrich-Alexander-Universität Erlangen-Nürnberg

Hitomi Collaboration 2016, Nature, 535, 117

Hitomi Collaboration 2017, Nature, 551, 478 (Z paper)

Hitomi Collaboration 2018a, PASJ, 70, 9 (V paper)

Hitomi Collaboration 2018b, PASJ, 70, 11 (T paper)

Hitomi Collaboration 2018c, PASJ, 70, 12 (A paper)

Hitomi Collaboration 2018d, PASJ, 70, 13

Kaastra, J. S., Lieu, R., Mittaz, J. P. D., Bleeker, J. A. M., Mewe, R., Colafrancesco, S., & Lockman, F. J. 1999, ApJ, 519, L119

Kaastra, J. S., Mewe, R., & Nieuwenhuijzen, H. 1996, in UV and X-ray Spectroscopy of Astrophysical and Laboratory Plasmas, ed. K. Yamashita & T. Watanabe (Tokyo: Universal Academy Press), 411

Kahn, S. M., et al. 2003, in ASP Conf. Ser., 301, Matter and Energy in Clusters of Galaxies, ed. S. Bowyer & C.-Y. Hwang (San Francisco: ASP), 23

Kalberla, P. M. W., Burton, W. B., Hartmann, D., Arnal, E. M., Bajaja, E., Morras, R., & Pöppel, W. G. L. 2005, A&A, 440, 775

Kelley, R. L., et al. 2016, Proc. SPIE, 9905, 99050V

Lodders, K., & Palme, H. 2009, Meteorit. Planet. Sci. Suppl., 72, 5154

Mathews, W. G., Buote, D. A., & Brighenti, F. 2001, ApJ, 550, L31

Matsushita, K., Sakuma, E., Sasaki, T., Sato, K., & Simionescu, A. 2013, ApJ, 764, 147

Molendi, S., Matt, G., Antonelli, L. A., Fiore, F., Fusco-Femiano, R., Kaastra, J., Maccarone, C., & Perola, C. 1998, ApJ, 499, 608

Ogorzalek, A., et al. 2017, MNRAS, 472, 1659

Pinto, C., et al. 2016, MNRAS, 461, 2077

Porter, F. S., et al. 2016, Proc. SPIE, 9905, 99050W

Rudolph, J. K., et al. 2013, Phys. Rev. Lett., 111, 103002

Sakelliou, I., et al. 2002, A&A, 391, 903

Salomé, P., Combes, F., Revaz, Y., Downes, D., Edge, A. C., & Fabian, A. C. 2011, A&A, 531, A85

Sanders, J. S., & Fabian, A. C. 2006, MNRAS, 370, 63

Sanders, J. S., Fabian, A. C., Allen, S. W., & Schmidt, R. W. 2004, MNRAS, 349, 952

Savin, D. W., et al. 2008, Canadian J. Phys., 86, 209

Savin, D. W., Beiersdorfer, P., Kahn, S. M., Beck, B. R., Brown, G. V., Gu, M. F., Liedahl, D. A., & Scofield, J. H. 2000, Rev. Sci. Instrum., 71, 3362

Sazonov, S. Y., Churazov, E. M., & Sunyaev, R. A. 2002, MNRAS, 333, 191

Shigeyama, T. 1998, ApJ, 497, 587

Smith, R. K., Brickhouse, N. S., Liedahl, D. A., & Raymond, J. C. 2001, ApJ, 556, L91

Takahashi, et al. 2017, JATIS submitted

Tsujimoto, M., et al. 2018, PASJ, 70, 14

Urban, O., et al. 2014, MNRAS, 437, 3939

Urdampilleta, I., Kaastra, J. S., & Mehdipour, M. 2017, A&A, 601, A85

Watanabe, H., Currell, F. J., Kuramoto, H., Li, Y. M., Ohtani, S., O'Rourke, B., & Tong, X. M. 2001, J. Phys. B, 34, 5095

Werner, N., Urban, O., Simionescu, A., & Allen, S. W. 2013, Nature, 502, 656

Werner, N., Zhuravleva, I., Churazov, E., Simionescu, A., Allen, S. W., Forman, W., Jones, C., & Kaastra, J. S. 2009, MNRAS, 398, 23

Wong, K. L., Beiersdorfer, P., Reed, K. J., & Vogel, D. A. 1995, Phys. Rev. A, 51, 1214

Xu, H., et al. 2002, ApJ, 579, 600

Zhang, H. L., & Sampson, D. H. 1990, Phys. Rev. A, 42, 5378

Zhuravleva, I., et al. 2013, MNRAS, 435, 3111

Zhuravleva, I. V., Churazov, E. M., Sazonov, S. Y., Sunyaev, R. A., & Dolag, K. 2011, Astron. Lett., 37, 141

Zhuravleva, I. V., Churazov, E. M., Sazonov, S. Y., Sunyaev, R. A., Forman, W., & Dolag, K. 2010, MNRAS, 403, 129